Electronic Research Archive

https://www.aimspress.com/journal/era

ERA, 34(9): 6999–7026.
DOI: 10.3934/era.2026303
Received: 05 June 2026
Revised: 20 July 2026
Accepted: 24 July 2026
Published: 14 August 2026

Research article

A new 5D hyperjerk system: hyperchaos, Hopf bifurcation, synchronization, circuit design and an encryption application

Junhong Li[1,*], **Ning Cui**[1] **and Liang Wang**[2]

[1] School of Mathematics and Statistics, Hanshan Normal University, Chaozhou, Guangdong 521041, China

[2] Coordinated Innovation Center for Computable Modelling in Management Science, Tianjin University of Finance and Economics, Tianjin 300222, China

* **Correspondence:** Email: jhli2011@163.com.

Abstract: Different from the classical triangular-structure hyperjerk forms, this work constructed a new five-dimensional (5D) hyperjerk system from a novel perspective and analyzed its dissipativity as well as the stability of the equilibrium point. By employing methods such as Lyapunov exponents, bifurcation diagrams, the 0-1 test, and Poincaré sections, the existence of a hyperchaotic attractor and the rich dynamical behaviors of the system were revealed. Based on normal form theory and symbolic computations, the existence of Hopf bifurcations and the stability of the bifurcation solutions were further investigated, and numerical examples were provided to validate the theoretical findings. By incorporating Lyapunov functions, we designed a suitable nonlinear controller that achieves global asymptotic synchronization of the hyperchaotic system. Simulation results demonstrated that the drive-response system achieves synchronization rapidly. In addition, an electronic circuit design scheme for the 5D hyperchaotic system was presented. The circuit simulation results were in good agreement with the numerical simulations, thereby verifying the physical realizability of the system. Finally, the practical application of the proposed hyperchaotic system in information encryption and decryption was explored. Based on this 5D hyperchaotic hyperjerk system, we developed encryption and decryption algorithms. From the analysis results of multiple metrics, including the correlation coefficient, information entropy, key space, number of pixel change rate, and unified average changing intensity, the proposed algorithm demonstrated favorable confidentiality and robust security performance.

Keywords: hyperchaotic hyperjerk system; Hopf bifurcation; hyperchaos synchronization; hyperchaotic circuit; hyperchaos encryption

1. Introduction

As a complex phenomenon ubiquitous in nonlinear dynamical systems, chaos is characterized by pseudo-randomness, ergodicity, and sensitivity to initial conditions, which endow it with significant applications in fields such as engineering [1], physics [2], and economics [3]. Since Lorenz discovered the first chaotic system [4], decades of research have witnessed the successive proposal of a series of classical chaotic models, including the Rossler system [5], the jerk system [6], the Chen system [7], and the Lü system [8]. Subsequently, various new chaotic systems have continued to emerge (see [9–11] and the references therein). These continuously expanding research achievements have greatly enriched the theoretical framework of chaotic dynamics [12]. With the deepening of nonlinear dynamics theory and the increasing demands of practical applications, chaos research has gradually evolved from low-dimensional to high-dimensional systems, and from simple chaos to hyperchaos. The essential characteristic that distinguishes a hyperchaotic system from an ordinary chaotic system is the presence of two or more positive Lyapunov exponents. This indicates that the system exhibits orbital divergence in more directions. Consequently, compared with ordinary chaotic systems, hyperchaotic systems possess more complex dynamical behaviors, higher unpredictability, and stronger randomness [13, 14]. This complexity endows hyperchaotic systems with greater application potential in nonlinear science-related fields such as secure communication [15], image encryption [16], and nonlinear circuits [17].

Among the various structures of chaotic systems, the jerk system has attracted widespread attention due to its distinctive mathematical form and rich dynamical connotations. A jerk system originally refers to a differential equation that includes the third derivative of displacement, with its physical background rooted in the description of the rate of change of acceleration. Generally, jerk systems of fourth order or higher are referred to as hyperjerk systems [18, 19]. As an important extension of the jerk system, hyperjerk systems possess the dual characteristics of structural simplicity and rich dynamical behaviors, which has led to sustained attention in the field of nonlinear dynamics in recent years. Focusing on such systems, researchers have conducted extensive work in aspects such as system construction, dynamical analysis, synchronization control, circuit implementation, and application exploration, achieving a series of significant advancements. In terms of system construction and dynamical analysis, researchers have focused on developing hyperjerk systems with novel characteristics. Vaidyanathan et al. [20] proposed a four-dimensional chaotic hyperjerk system with a half-line of equilibrium points. Due to the existence of infinitely many equilibrium points, this system exhibits hidden attractor characteristics, and bifurcation diagrams along with Lyapunov exponent spectra reveal multistability and coexisting attractor phenomena. Rajagopal et al. [21] proposed a multistable chaotic hyperjerk system with both self-excited and hidden attractors. Jiang et al. [22] investigated a class of hyperjerk systems exhibiting antimonotonicity, revealing rich dynamical behaviors including period-doubling cascades as a route to chaos, intermittency regimes, antimonotonicity, and boundary crises through analytical methods and numerical calculations. The coexisting dynamics were confirmed via basins of attraction, bifurcation diagrams, Lyapunov exponent spectra, and phase portraits. Zambrano-Serrano and Anzo-Hernández [23] derived a novel chaotic oscillator from generalized four-dimensional autonomous jerk systems, whose core feature is the presence of antimonotonicity in a region of the parameter space, where periodic orbits are generated and subsequently annihilated through inverse period-doubling bifurcations. Synchronization conditions were established using the Lyapunov function method. Leutcho et al. [24] proposed a novel hyperjerk circuit exhibiting mixed-mode oscillation phenomena, introducing the concept of "bifurcation bubbles" and the coexistence of two or three asymmetric mixed-mode bursting oscillations, with experimental validation supporting the theoretical analysis. Taha et al. [25] investigated the Hopf bifurcation and periodic solutions of a class of 5D hyperjerk systems. Bao et al. [26] constructed a parameter-free memristive hyperjerk system, utilizing the initial condition of the memristor internal state as a bifurcation parameter to reveal initial condition-boosted chaotic bubble phenomena, demonstrating infinitely many coexisting attractors with extreme multistability. A digital hardware platform verified the memristor initial condition-dependent chaotic bubbles. In synchronization control and applications, Zhang et al. [27] proposed a terminal sliding-mode control method based on fuzzy recurrent neural networks for unmodeled hyperjerk systems subject to parameter perturbations and external disturbances, achieving finite-time chattering-free projective synchronization. Simulation results validated the effectiveness of the proposed method. Vaidyanathan et al. [28] presented a new chaotic hyperjerk system with two exponential nonlinearities, designed an adaptive backstepping controller for synchronization, completed an actual circuit design, and applied the system to random number generation, image encryption, and sound steganography, demonstrating broad application prospects. Regarding hyperchaotic behavior research, Wang et al. [29] pointed out that although various hyperjerk systems have been reported, only a few can exhibit hyperchaotic behavior. Furthermore, research progress on high-dimensional hyperchaotic systems remains quite limited, and their dynamical behaviors are not yet fully understood. Therefore, undertaking new research on hyperchaotic systems remains a challenging task, which motivates us to further explore certain subtle characteristics of hyperchaos, with the aim of revealing the true geometric structures of hyperchaotic attractors [30, 31]. Based on this, our work constructs a new 5D hyperchaotic hyperjerk system and further investigates its dynamical characteristics and applications.

The rest of this paper is organized as follows. Section 2 introduces the proposed 5D hyperchaotic hyperjerk system. Through theoretical analysis, symbolic computations, and numerical simulations, the dissipativity and equilibrium point stability of the system are investigated. Furthermore, the characteristics of the hyperchaotic attractor, as well as the existence of a Hopf bifurcation and the stability conditions of the bifurcation solutions, are explored in detail. In Section 3, a Lyapunov function and a corresponding nonlinear controller are designed to achieve hyperchaotic synchronization and simulation results are provided to validate its effectiveness. Section 4 describes the electronic circuit implementation of the 5D hyperchaotic system and the circuit simulation results confirm its physical realizability. Section 5 presents encryption and decryption algorithms based on the proposed 5D hyperchaotic hyperjerk system, and their confidentiality and security are illustrated through case simulations. Finally, the conclusions are summarized in Section 6.

2. Model and dynamical analysis

A new 5D hyperchaotic hyperjerk system is described as follows:

$$\begin{cases} \dot{x} = x_1, \\ \dot{x}_1 = a x_2, \\ \dot{x}_2 = -a_1 x - a_2 x_1 - a_3 x_2 + a_4 x_3, \\ \dot{x}_3 = -a_5 x_4 - a_6 x_3, \\ \dot{x}_4 = (x_1 + a x_2 + a) x_2 + (x + x_1) \dot{x}_2 - a_0 x_4, \end{cases} \tag{2.1}$$

where a_i, $i = 0, 1, 2, 3, 4, 5, 6$, are positive parameters. x, x_1, x_2, x_3, x_4 are the state variables. (2.1) can be equivalently written as the following fifth-order differential equation:

$$x^{(5)} = -(a_3 + a_6 + a_0)x^{(4)} - [a a_2 + a_3 a_6 + \tfrac{a_4 a_5 (x + \dot{x})}{a} + a_0(a_3 + a_6)]\dddot{x} - [a(a_1 + a_2 a_6) + \tfrac{a_4 a_5 (\dot{x} + a)}{a}$$
$$+ a_0(a a_2 + a_3 a_6)]\ddot{x} - [a a_1 a_6 + a a_0 (a_1 + a_2 a_6)]\dot{x} + a^2 a_1 a_6 a_0\, x - \tfrac{a_4 a_5}{a}[\dot{x}\ddot{x} + (\ddot{x})^2].$$

The system in [23] can be regarded as a special case of (2.1). Indeed setting $a = 1$, $a_5 = 1$, $a_0 = 0$, and $x_4 = -f(x, x_1, x_2) = x_1 + (x + x_1)x_2 + \beta$ transforms (2.1) into the system described in [23]. Thus, the 4D system in [23] is a special case of the proposed 5D system. Furthermore, [23] constructed a hyperjerk system by introducing a control variable into the third equation, whereas system (2.1) herein constructs a new hyperjerk system by simultaneously introducing control variables into both the third and fourth equations. The increase in both dimension and variable constraints renders the dynamical behaviors of the proposed system more complex.

2.1. Dissipativity

The divergence of the vector field of states of (2.1) is

$$\nabla V = \frac{\partial \dot{x}}{x} + \frac{\partial \dot{x}_1}{x_1} + \frac{\partial \dot{x}_2}{x_2} + \frac{\partial \dot{x}_3}{x_3} + \frac{\partial \dot{x}_4}{x_4} = -a_3 - a_6 - a_0 < 0.$$

Thus, (2.1) is dissipative.

2.2. Equilibrium point

Obviously, (2.1) has only one zero-equilibrium point $E_0 = (0, 0, 0, 0, 0)$ and the characteristic equation of the Jacobian matrix at E_0 is

$$f(\lambda) = (\lambda^2 + (a_6 + a_0)\lambda + a_6 a_0)(\lambda^3 + a_3\lambda^2 + a a_2 \lambda + a a_1) + a a_4 a_5 \lambda^2. \tag{2.2}$$

Remark 1. *The zero-equilibrium point E_0 is asymptotically stable when*

$$b_4 b_3 - b_2 > 0,$$
$$b_4 b_3 b_2 - b_4^2 b_1 - b_2^2 + b_4 b_0 > 0,$$
$$b_4 b_1 b_2 b_3 - b_4^2 b_3 b_0 - b_4^2 b_1^2 + 2 b_4 b_0 b_1 - b_1^2 b_2^2 + b_2 b_3 b_0 - b_0^2 > 0,$$

where

$$b_4 = a_3 + a_6 + a_0,$$
$$b_3 = a_3 a_6 + a_3 a_0 + a_6 a_0 + a a_2,$$
$$b_2 = a_3 a_6 a_0 + a a_4 a_5 + a a_2 (a_6 + a_0) + a a_1,$$
$$b_1 = a a_2 a_6 a_0 + a a_1 (a_6 + a_0),\ b_0 = a a_1 a_6 a_0.$$

Otherwise, if some roots of (2.2) *have nonnegative real parts, then E_0 is unstable.*

2.3. *Existence of hyperchaos*

For the parameter values

$$(a, a_1, a_2, a_3, a_4, a_5, a_6, a_0) = (5.99, 2.55, 0.55, 1.99, 0.51, 0.9, 0.55, 0.0002),$$

the Lyapunov exponents of (2.1) are calculated as

$$L_1 = 0.13,\ L_2 = 0.10,\ L_3 = 0.00,\ L_4 = -0.54,\ L_5 = -2.23,$$

which indicates that the hyperjerk system (2.1) is hyperchaotic.

Here, the Wolf algorithm [32] is employed to calculate the Lyapunov exponents, with the simulation duration set to 10^6 seconds and the error tolerance set to 10^{-12}. The hyperchaotic attractors of (2.1) on different cross sections are depicted in Figures 1 and 2. To further illustrate the complex dynamical phenomena of the system, Figures 3 and 4 show the Poincaré sections of (2.1) on the $x_1 - x_4$ plane, the $x_3 - x_4$ plane, and the $x_2 - x_4$ plane, respectively. Figure 5 displays the $p - s$ dynamics obtained from the $0 - 1$ test. Here, p and s denote the two translation variables of the time series corresponding to variable x_3, respectively. The motion trajectories of the system on the $p - s$ plane resemble unbounded Brownian motion. The results presented in Figures 3–5 further confirm the complex dynamical characteristics of the system [13, 33].

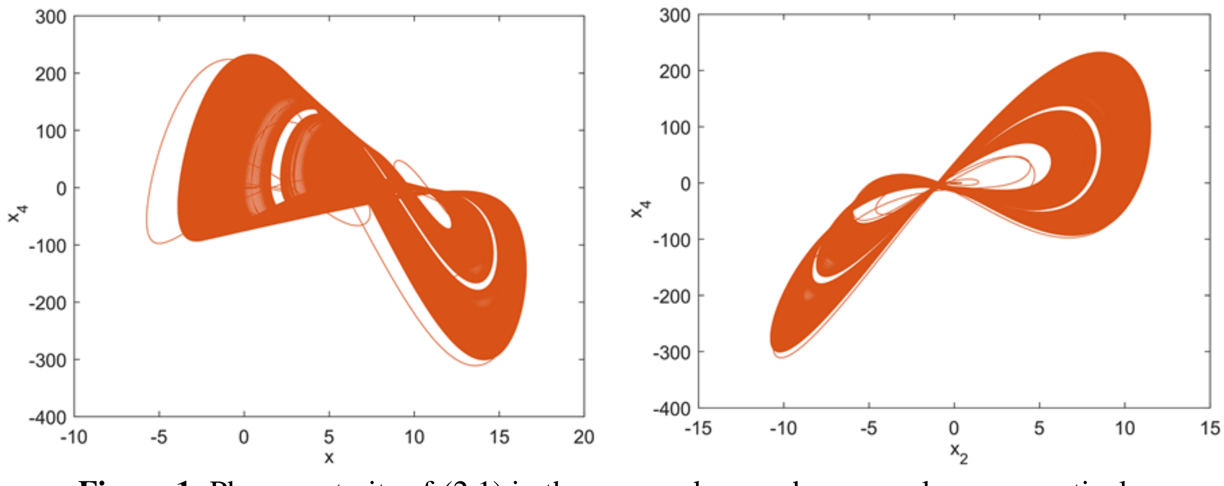

Figure 1. Phase portraits of (2.1) in the $x - x_4$ plane and $x_2 - x_4$ plane, respectively.

All parameters except a are fixed as above. When a varies from 0.9 to 9.9, the corresponding Lyapunov exponent spectrum and bifurcation diagram are presented in Figures 6 and 7, respectively. As shown in the figures, when a is close to 2 and continues to increase, system (2.1) enters a hyperchaotic state. Therefore, hyperchaotic phenomena can occur in the system under various parameter values. Moreover, the system exhibits different hyperchaotic characteristics under different parameter conditions.

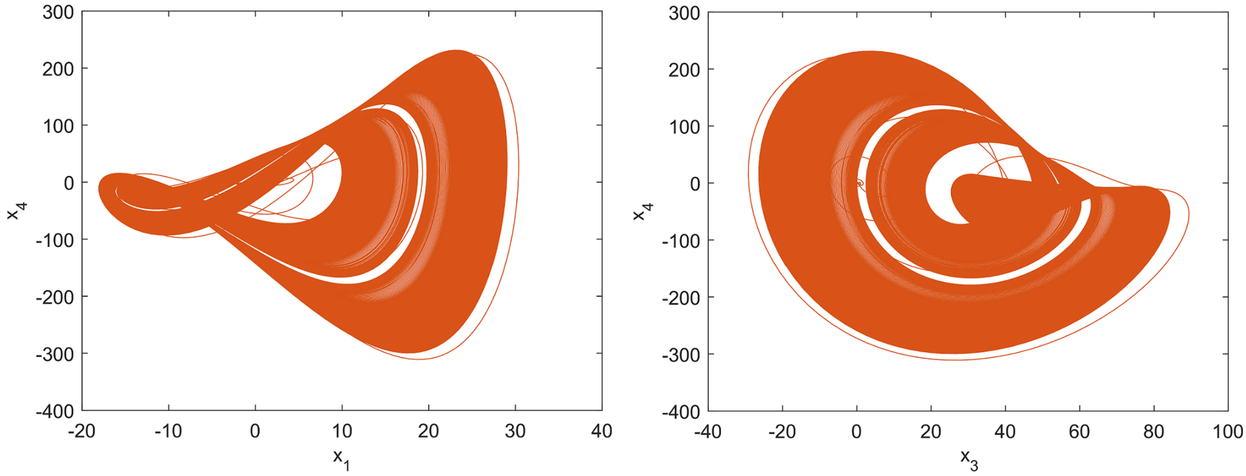

Figure 2. Phase portraits of (2.1) in the $x_1 - x_4$ plane and $x_3 - x_4$ plane, respectively.

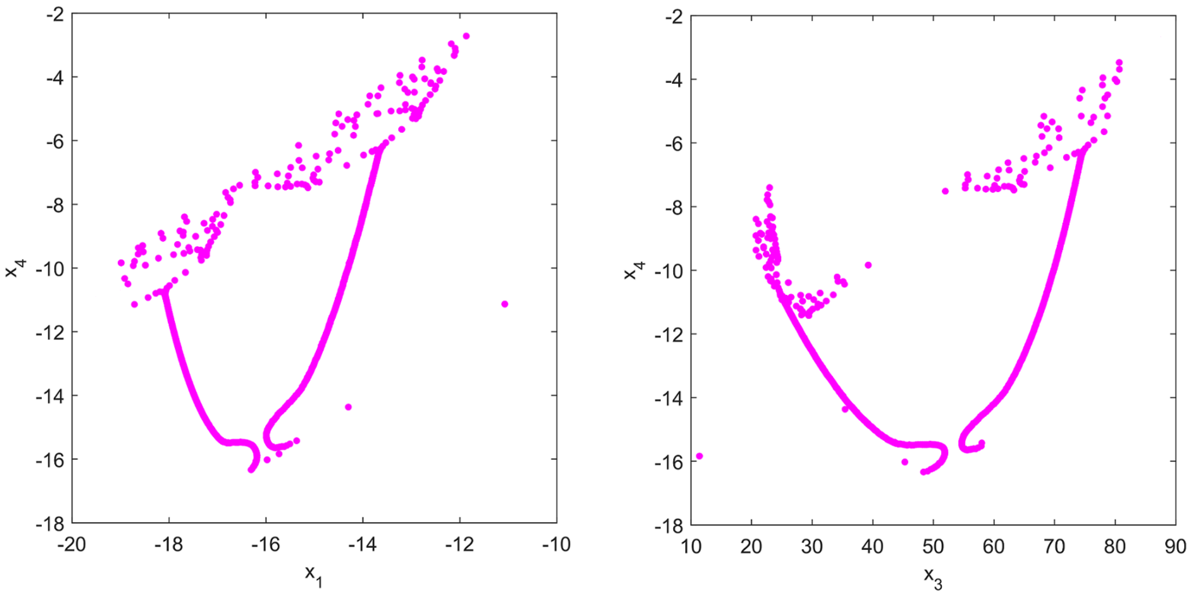

Figure 3. Poincaré mappings on the $x_1 - x_4$ plane and $x_3 - x_4$ plane, respectively.

It should be noted that variations in system parameters other than a can also induce complex dynamical behaviors. To verify this conclusion, Figures 8 and 9 present the single-parameter bifurcation patterns of the hyperjerk system with all other parameters fixed: Figure 8 corresponds to the case where parameter $a_3 \in [0.7, 3]$ and Figure 9 corresponds to $a_1 \in [2, 5.5]$. As shown in Figure 8, when a_3 lies in the interval $[0.97, 1.81]$, the complexity of the system's dynamical behavior is significantly higher than for values outside this range. The results in Figure 9 indicate that as a_1 increases, the system complexity gradually rises, exhibiting a stepwise increase across the three intervals $[2, 2.49]$, $(2.49, 3.91]$, and $(3.91, 5.5]$.

Specifically, the Lyapunov exponent spectrum corresponding to Figures 8 and 9 are presented in Figures 10 and 11, respectively. The right panel of Figure 10 illustrates the spectra of the first and second Lyapunov exponents for the system as parameter a_3 ranges over the interval $[0.97, 1.81]$. This result corroborates the findings presented in Figure 8, further underscoring the complex dynamical behavior of the system within this parameter regime. Inset s in Figure 11 provides a locally magnified view of the third Lyapunov exponent over the interval $[5, 5.5]$, which serves to further corroborate the hyperchaotic characteristics of the system. A consistent color scheme is adopted in Figures 6 and 11: curves in magenta, green, red, cyan, and blue correspond to the first through fifth Lyapunov exponents of (2.1), respectively.

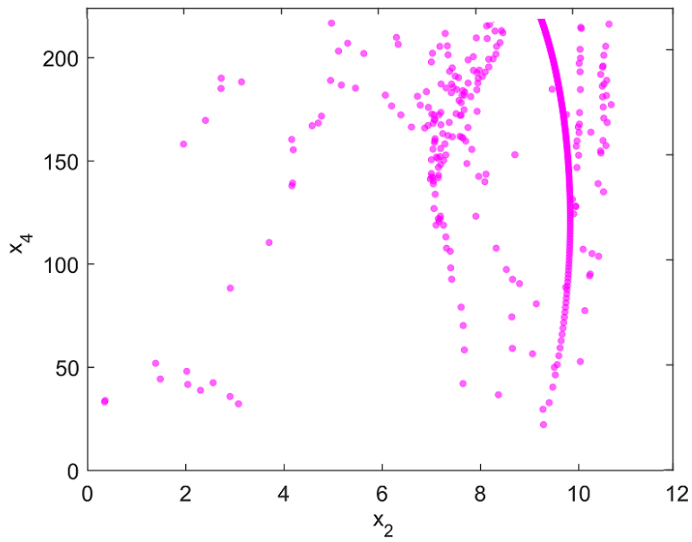

Figure 4. Poincaré mapping on the $x_2 - x_4$ plane.

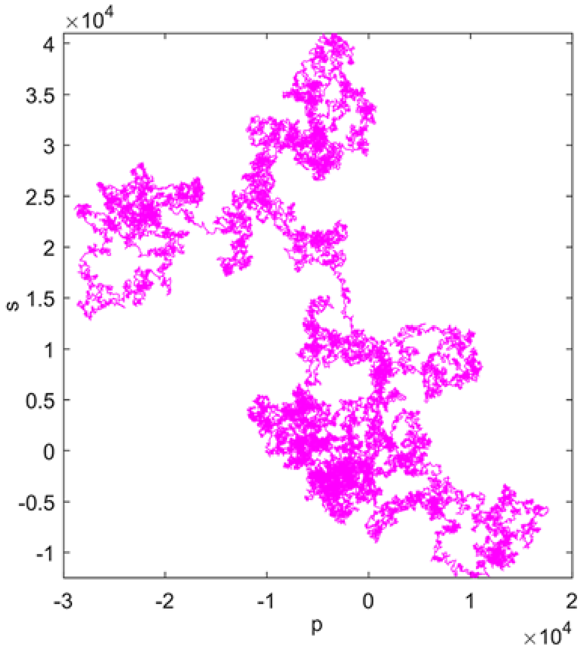

Figure 5. The $p - s$ phase diagram for the $0 - 1$ test.

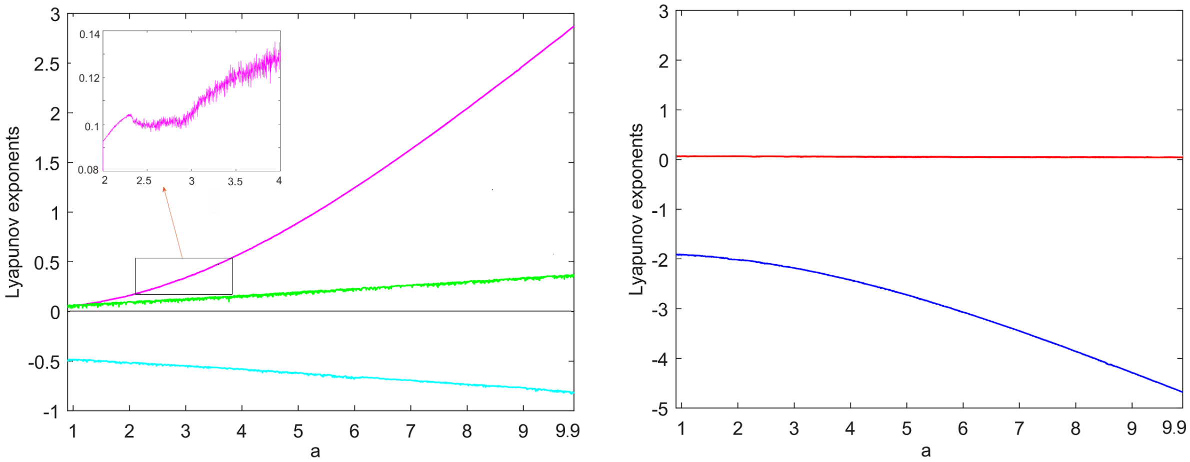

Figure 6. The Lyapunov exponents of (2.1).

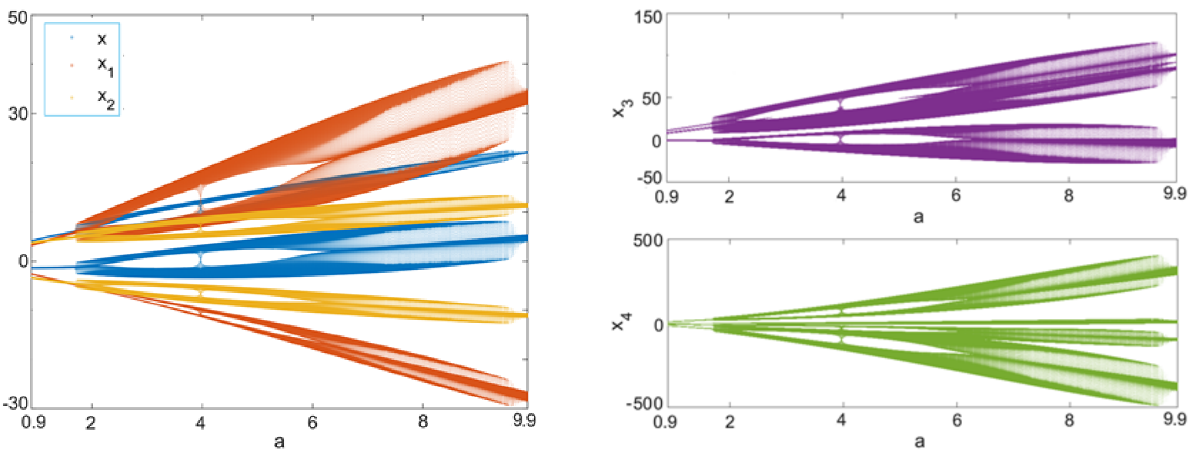

Figure 7. The bifurcation diagrams of $x,\ x_1,\ x_2,\ x_3,\ x_4$ corresponding to Figure 6.

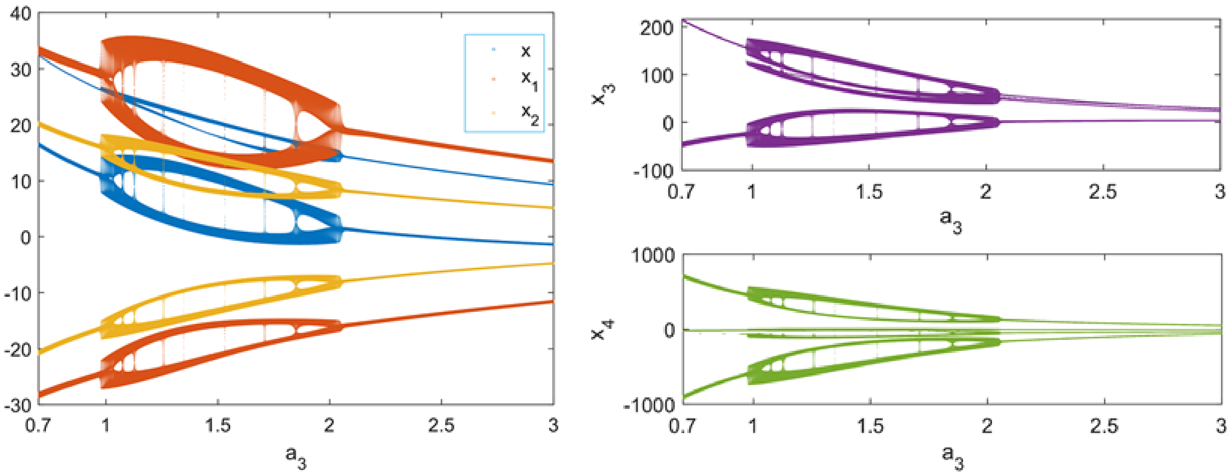

Figure 8. Bifurcation diagram of (2.1) with $a_3 \in [0.7, 3]$.

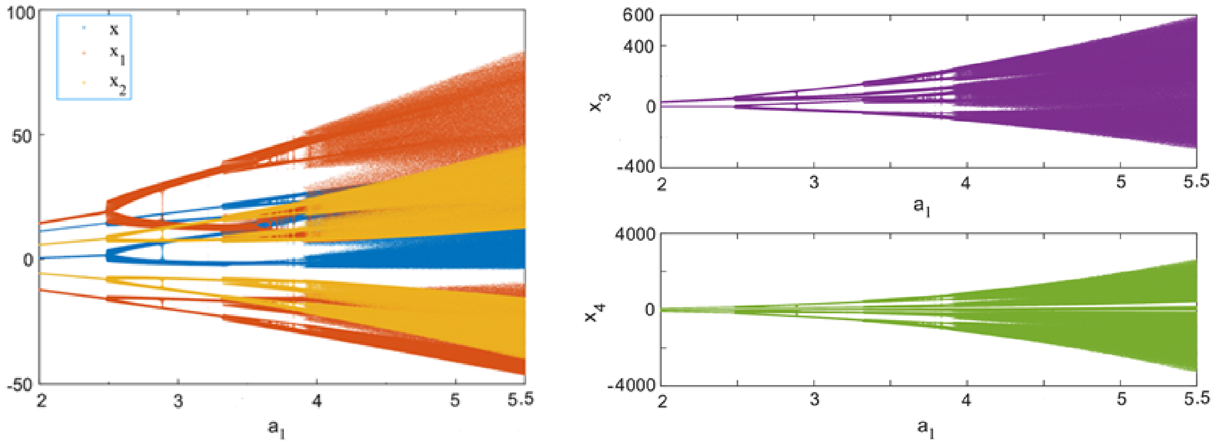

Figure 9. Bifurcation diagram of (2.1) with $a_1 \in [2, 5.5]$.

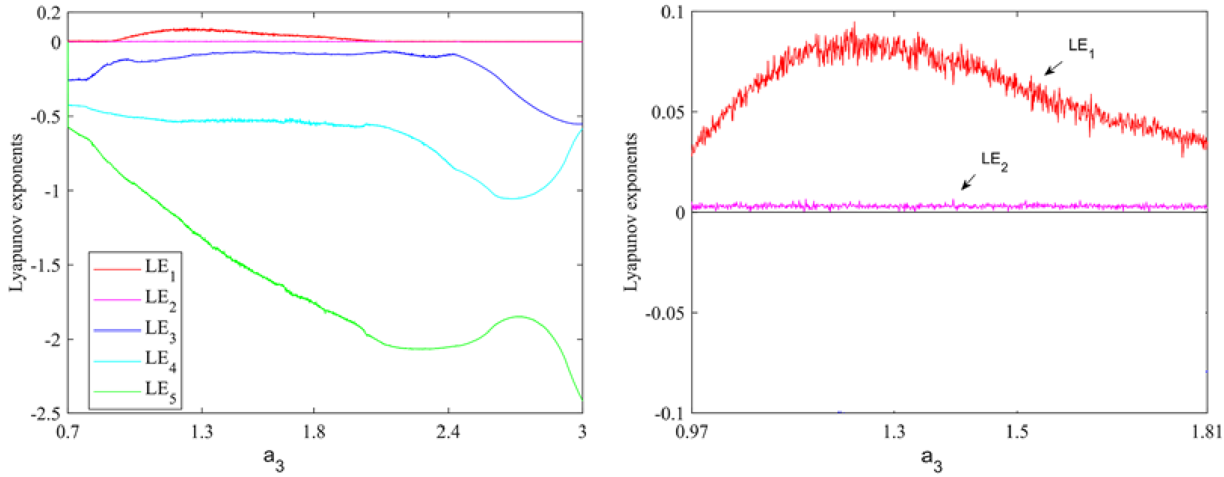

Figure 10. Lyapunov exponent spectrum corresponding to Figure 8.

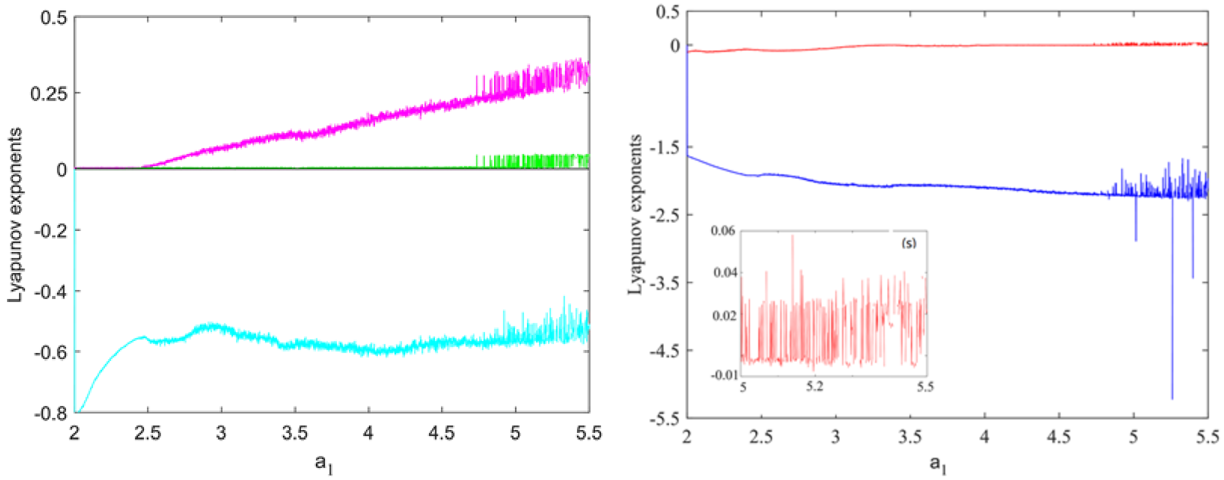

Figure 11. Lyapunov exponent spectrum corresponding to Figure 9.

2.4. Existence of Hopf bifurcations

Calculation shows that when the parameters satisfy the following conditions:

$$b_1b_3b_4^2-(b_0b_3+b_1b_2)b_4+b_0b_2>0,$$
$$(b_4b_1-b_0)^2-b_3(b_4b_1-b_0)(b_4b_3-b_2)+b_1(b_4b_3-b_2)^2=0,$$

Equation (2.2) has a purely imaginary root $\lambda = \mathrm{i}\omega$ ($\omega \in \mathbb{R}^+$), where $\omega = \sqrt{\frac{b_4b_1-b_0}{b_4b_3-b_2}}$. For simplicity, we assume $b_0 = b_1(b_2-b_1b_4)$, $b_3 = b_1+1$, $b_1 \neq 1$, which yields

$$\omega = \sqrt{b_1}, a_5 = a_5^* = \frac{1}{aa_4}\left(\frac{aa_1a_0a_6}{b_1} - a_0a_3a_6 - aa_2\left(a_0+a_6\right) - aa_1 + b_1b_4\right).$$

When $27b_0^2+18b_0b_1b_4+4b_1^2 \leq b_1b_4^2(4b_0b_4+b_1)$, Eq (2.2) has three negative real roots $\lambda_{3,4,5}$ and a pair of purely imaginary roots $\lambda_{1,2} = \pm\sqrt{b_1}i$. Furthermore, we have

$$\mathrm{Re}(\lambda'(a_5^*))|_{\lambda=i\omega} = \frac{aa_4b_1^3(b_1-1)}{2b_1^3(b_1-1)^2+2b_0^2} \neq 0.$$

Thus, the first condition and second condition for a Hopf bifurcation [34] are satisfied. Consequently, as a_5 varies and passes through the critical value a_5^*, (2.1) undergoes Hopf bifurcations at E_0.

Next, we use the method described in [35] to calculate the first Lyapunov coefficient at E_0. When $a_5 = a_5^*$, the Jacobian matrix at E_0 and its inverse matrix are

$$J = \begin{bmatrix} 0 & 1 & 0 & 0 & 0 \\ 0 & 0 & a & 0 & 0 \\ -a_1 & -a_2 & -a_3 & a_4 & 0 \\ 0 & 0 & 0 & -a_6 & -a_5^* \\ 0 & 0 & a & 0 & -a_0 \end{bmatrix},$$

$$J^{-1} = \begin{bmatrix} -\frac{a_2}{a_1} & -\frac{a_4a_5^*a+a_3a_0a_6}{a_1aa_6a_0} & -\frac{1}{a_1} & -\frac{a_4}{a_6a_1} & \frac{a_4a_5^*}{a_0a_6a_1} \\ 1 & 0 & 0 & 0 & 0 \\ 0 & \frac{1}{a} & 0 & 0 & 0 \\ 0 & -\frac{a_5^*}{a_0a_6} & 0 & -\frac{1}{a_6} & \frac{a_5^*}{a_0a_6} \\ 0 & \frac{1}{a_0} & 0 & 0 & -\frac{1}{a_0} \end{bmatrix}.$$

Through complex calculations, one obtains

$$\eta = \begin{bmatrix} -ia \\ -ia\omega \\ \omega^2 \\ -\frac{ia\omega\, a_2 - i\omega^3 - \omega^2a_3 + aa_1}{a_4} \\ -\frac{a\omega^2(i\omega-a_0)}{\omega^2+a_0{}^2} \end{bmatrix},$$

$$\theta = \begin{bmatrix} -\frac{a_1(i\theta_1-\theta_0)}{\omega} \\ -\frac{(ia_1+\omega a_2)(i\theta_1-\theta_0)}{\omega^2} \\ \theta_1 + i\theta_0 \\ -\frac{a_4(ia_6-\omega)(i\theta_1-\theta_0)}{\omega^2+a_6{}^2} \\ \frac{\left(-i\omega^2 a_3+iaa_1+a\omega a_2-\omega^3\right)(i\theta_1-\theta_0)}{\omega^2 a} \end{bmatrix},$$

which satisfy $J\eta = i\omega\eta$, $J^T\theta = -i\omega\theta$, and $< \theta, \eta >= 1$, where $\theta_0 = \frac{\theta_{01}\omega}{\theta_{02}}$, $\theta_1 = \frac{\theta_{11}\omega^2}{\theta_{12}}$, and the expressions of θ_{ks} ($k = 0, 1$, $s = 1, 2$) can be seen in Appendix. Furthermore, one has the bilinear in terms of η as

$$B(\eta, \eta) = \begin{pmatrix} 0, & 0, & 0, & 0, & \eta_1 + \eta_0 i \end{pmatrix}^T,$$

$$B(\eta, \bar{\eta}) = \begin{pmatrix} 0, & 0, & 0, & 0, & \eta_3 + \eta_2 i \end{pmatrix}^T,$$

where $\eta_0 = 4\,a\omega^3 a_3 - 2\,a_1 a^2\omega - 2\,a\omega^3 + 4\,a_3 a\omega^2 - 2\,a_1 a^2$, $\eta_1 = 2\,a_1 a^2\omega - 2\,a\omega^3 + 2\,a_1 a^2$,

$$\eta_3 = 3\,a\omega^4 + (2\,a - 2\,a_3 + 1)\omega^3 + a_2 a^2\omega^2 + (a_1 a - a_1 a^2 + a_2 a^2)\omega - 2\,a_1 a^2,$$

$$\eta_2 = -\omega^4 + (2\,aa_3 - a)\omega^3 + aa_2\omega^2 + (aa_2 - a_1 a^2 + a_1 a)\omega.$$

Since there are no cubic terms in system (2.1), the first Lyapunov coefficient at E_0 is:

$$l = \frac{1}{2\omega} Re[-2\theta^T B(\eta, J^{-1}B(\eta, \bar{\eta})) + \theta^T B(\bar{\eta}, (2i\omega I - J)^{-1} B(\eta, \eta))] = -\frac{\delta}{2\omega a a_0 a_1 a_6}\left[\sum_{k=0}^{10} \delta_k \omega^k\right],$$

where I denotes the 5th-order identity matrix and the expressions of δ, δ_j ($j = 0, 1, ..., 10$) can be seen in Appendix. Thus, we derive the following conclusions.

Theorem 1. *(I) Assume that* $b_0 = b_1(b_2 - b_1 b_4)$, $b_3 = b_1 + 1 \neq 2$, $9b_1 b_2 b_4^2(b_1 b_2 + 2) + 4 \leq b_4^2(1 + b_1 b_2 b_4^2)$. *Then, when* $l < 0$ *(resp.,* $l > 0$*), the Hopf bifurcation is supercritical (resp., subcritical) and a stable (resp., unstable) periodic orbit bifurcating from* E_0 *exists for sufficiently small* $|a_5 - a_5^*| > 0$.

(II) When $(b_1 b_4 - b_0)(b_3 b_4 - b_2) \leq 0$, (2.1) *exhibits no Hopf bifurcation.*

Take $(a, a_0, a_1, a_2, a_3, a_4, a_6) = (1, 2, 24, 26, 1, 2, 6)$, and as a_5 varies and passes through the critical value $a_5^* = 4$, (2.1) undergoes Hopf bifurcations at E_0. A bifurcating periodic solution exists for $a_5 = 4.009$ and the corresponding periodic orbit is depicted in Figure 12. Here, $l \approx -1.28 \times 10^{13} < 0$, which indicates that the Hopf bifurcation is supercritical and that a stable periodic orbit bifurcates from E_0.

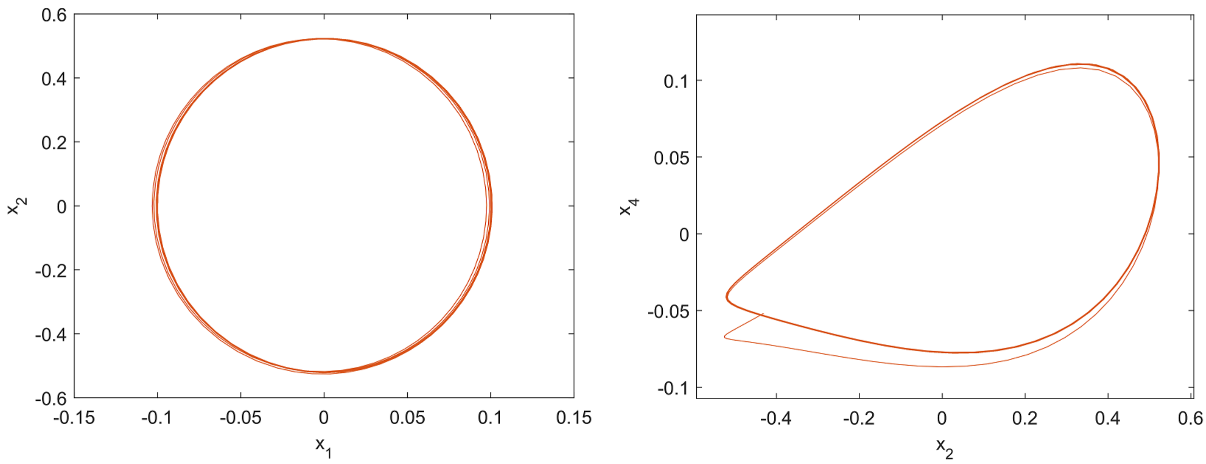

Figure 12. Phase portraits of (2.1) in the $x_1 - x_2$ plane and $x_2 - x_4$ plane, respectively.

3. Hyperchaos synchronization

In this section, we investigate the hyperchaos synchronization of the hyperjerk system using nonlinear feedback control. Let the drive system be (2.1) and the response system is

$$\begin{cases} \dot{y} = y_1 + c_1, \\ \dot{y}_1 = ay_2 + c_2, \\ \dot{y}_2 = -a_1 y - a_2 y_1 - a_3 y_2 + a_4 y_3 + c_3, \\ \dot{y}_3 = -a_5 y_4 - a_6 y_3 + c_4, \\ \dot{y}_4 = (y_1 + ay_2 + a)y_2 + (y + y_1)\dot{y}_2 - a_0 y_4 + c_5, \end{cases} \tag{3.1}$$

where $(c_1, c_2, c_3, c_4, c_5)^T$ is the nonlinear controller to be designed. Subtracting system (2.1) from system (3.1) yields the following error system:

$$\begin{cases} \dot{e}_1 = e_2 + c_1, \\ \dot{e}_2 = ae_3 + c_2, \\ \dot{e}_3 = -a_1 e_1 - a_2 e_2 - a_3 e_3 + a_4 e_4 + c_3, \\ \dot{e}_4 = -a_5 e_5 - a_6 e_4 + c_4, \\ \dot{e}_5 = -ae_3^2 + e_{53} e_3 + e_{52} e_2 + e_{51} - a_0 e_5 + c_5, \end{cases} \tag{3.2}$$

where

$$e_1 = y - x, e_2 = y_1 - x_1, e_3 = y_2 - x_2, e_4 = y_3 - x_3, e_5 = y_4 - x_4,$$

$$e_{53} = 2\,ay_2 - ya_3 + a_3 e_1 + a_3 e_2 - a_3 y_1 + a - e_2 + y_1,$$

$$e_{52} = a_1 e_1 + a_2 e_1 + a_2 e_2 - ya_1 - ya_2 - 2\,a_2 y_1 - a_3 y_2 - a_4 e_4 + a_4 y_3 + y_2,$$

$$e_{51} = a_1 {e_1}^2 + (a_4 y_3 - 2\,ya_1 - a_1 y_1 - a_2 y_1 - a_3 y_2 - a_4 e_4)e_1 + (ya_4 + a_4 y_1)e_4.$$

Choose the Lyapunov function $V = {e_1}^2 + {e_2}^2 + v_3 e_3^2 + \frac{{a_4}^2 v_3}{4a_3 a_6} e_4^2 + v_5 e_5^2$,
where

$$v_3 = \frac{a(a_1 + 2\,a_2)}{{a_1}^2 + a_1 a_2 + {a_2}^2},$$

$$v_5 = \frac{(a_1 + 2\,a_2)a_5{}^2a_4{}^2a(5\,aa_1{}^2 + 5\,aa_1a_2 + 5\,aa_2{}^2 + 3\,a_1a_3 + 6\,a_2a_3)}{16a_3a_6a_0(5\,aa_1{}^4a_6 + 10\,aa_1{}^3a_2a_6 + 15\,aa_1{}^2a_2{}^2a_6 + 10\,aa_1a_2{}^3a_6 + 5\,aa_2{}^4a_6 + 1)}.$$

The nonlinear controllers are chosen as follows:

$$c_1 = -e_1,$$

$$c_2 = -e_2,$$

$$c_3 = -\frac{2a(a_1{}^2 + a_1a_2 + a_2{}^2)e_3}{a_1 + 2\,a_2},$$

$$c_4 = -\frac{e_4}{3\,a_1{}^3a_3 + 9\,a_1{}^2a_2a_3 + 9\,a_1a_2{}^2a_3 + 6\,a_2{}^3a_3},$$

$$\begin{aligned} c_5 = {} & ae_3{}^2 + [(y + y_1 - e_1 - e_2)a_3 - 2\,ay_2 - a - y_1 + e_2]e_3 - a_1e_1{}^2 + [(2\,y + y_1 - e_2)a_1 + y_1a_2 + y_2a_3 \\ & - y_3a_4 - a_2e_2 + a_4e_4]e_1 - a_2e_2{}^2 + [(e_4 - y_3)a_4 + ya_1 + ya_2 + 2\,y_1a_2 + y_2a_3 - y_2]e_2 - (ye_4 + e_4y_1)a_4 - e_5. \end{aligned}$$

Therefore, the time derivative of V along the trajectory of (3.2) is

$$\dot{V} = (e_1, e_2, e_3, e_4, e_5)C(e_1, e_2, e_3, e_4, e_5)^T,$$

where

$$C = \begin{pmatrix} -2 & 1 & -a_1v_3 & 0 & 0 \\ 1 & -2 & -a_2v_3 + a & 0 & 0 \\ -a_1v_3 & -a_2v_3 + a & -4a^2 - 2a_3v_3 & a_4v_3 & 0 \\ 0 & 0 & a_4v_3 & -\dfrac{v_3a_4^2(a_6v_0 + 1)}{2a_3a_6v_0} & -\dfrac{a_5v_3a_4^2}{4a_3a_6} \\ 0 & 0 & 0 & -\dfrac{a_5v_3a_4^2}{4a_3a_6} & -2v_5(1 + a_0) \end{pmatrix},$$

$$v_0 = 3\,a_1{}^3a_3 + 9\,a_1{}^2a_2a_3 + 9\,a_1a_2{}^2a_3 + 6\,a_2{}^3a_3.$$

By computing the leading principal minors of the matrix C, we obtain

$$C_{11} = -2 < 0,$$

$$C_{22} = 3 > 0,$$

$$C_{33} = -\frac{2a(5aa_1^2 + 5aa_1a_2 + 5aa_2^2 + 3a_1a_3 + 6a_2a_3)}{a_1^2 + a_1a_2 + a_2^2} < 0,$$

$$C_{44} = \frac{[15\,aa_1{}^2a_6(a_1{}^3+4\,a_1{}^2a_2+7\,a_1a_2{}^2+8\,a_2{}^3)+(75\,aa_2{}^4a_6+3)a_1+30\,aa_2{}^5a_6+6\,a_2]a_3+5\,aa_1{}^2+5\,aa_1a_2+5\,aa_2{}^2}{3a_6a_3{}^2(a_1{}^2+a_1a_2+a_2{}^2)^3} > 0,$$

$$C_{55} = -\frac{a^3a_5{}^2a_4{}^4C_0}{24(5\,aa_1{}^4a_6+10\,aa_1{}^3a_2a_6+15\,aa_1{}^2a_2{}^2a_6+10\,aa_1a_2{}^3a_6+5\,aa_2{}^4a_6+1)a_0(a_1{}^2+a_1a_2+a_2{}^2)^3a_6{}^2a_3{}^3} < 0,$$

$$
\begin{aligned}
C_0 = {} & 75a^2a_1{}^8a_3a_6 \\
& + (525a^2a_3a_6a_2 + 45aa_3{}^2a_6)a_1{}^7 \\
& + (1650a^2a_3a_6a_2{}^2 + 360aa_3{}^2a_6a_2)a_1{}^6 \\
& + (3225\,a^2a_3a_6a_2{}^3 + 1215\,aa_3{}^2a_6a_2{}^2 + 25\,a^2a_0 + 25\,a^2)a_1{}^5 \\
& + (4350\,a^2a_3a_6a_2{}^4 + 2340\,aa_3{}^2a_6a_2{}^3 + (100\,a^2a_0 + 100\,a^2)a_2 + (15\,aa_0 + 30\,a)a_3)a_1{}^4 \\
& + (4125\,a^2a_3a_6a_2{}^5 + 2925\,aa_3{}^2a_6a_2{}^4 + (175\,a^2a_0 + 175\,a^2)a_2{}^2 + (75\,aa_0 + 150\,a)a_3a_2 + 9\,a_3{}^2)a_1{}^3 \\
& + (2775\,a^2a_3a_6a_2{}^6 + 2430\,aa_3{}^2a_6a_2{}^5 + (200\,a^2a_0 + 200\,a^2)a_2{}^3 + (135\,aa_0 + 270\,a)a_3a_2{}^2 + 54\,a_3{}^2a_2)a_1{}^2 \\
& + (1200\,a^2a_3a_6a_2{}^7 + 1260\,aa_3{}^2a_6a_2{}^6 + (125\,a^2a_0 + 125\,a^2)a_2{}^4 + (120\,aa_0 + 240\,a)a_3a_2{}^3 + 108\,a_3{}^2a_2{}^2)a_1 \\
& + 300\,a^2a_2{}^8a_3a_6 + 360\,aa_2{}^7a_3{}^2a_6 + (50\,a^2a_0 + 50\,a^2)a_2{}^5 + (60\,aa_0 + 120\,a)a_3a_2{}^4 + 72\,a_2{}^3a_3{}^2,
\end{aligned}
$$

where $C_{jj}\,(j = 1, 2, 3, 4, 5)$ denote the leading principal minor of order j of matrix C. Therefore, C is negative definite. Hence, drive system (2.1) and response system (3.1) are globally asymptotically synchronized.

Figures 13 and 14 respectively present the phase portraits of (3.1) in the $y - y_4$ and $y_2 - y_4$ planes, and in the $y_1 - y_4$ and $y_3 - y_4$ planes. The time evolution of the state variables x, x_1, x_2, x_3, x_4 of drive system (2.1) and the state variables y, y_1, y_2, y_3, y_4 of response system (3.1) over the interval 0–20 s is detailed in Figure 15, where the horizontal axis represents time. Dynamics of synchronization errors e_1, e_5 and e_2, e_3, e_4 for the drive system and response system are given in Figures 16 and 17, respectively. The hyperchaotic parameters used here are the same as in subsection 2.3. The initial conditions for the drive system (2.1), response system (3.1), and error system (3.2) are set to $(0.05, 0.1, 0.01, 0.01, 0.02)$, $(0.06, 0.1, 0.01, 0.01, 0.03)$, and $(0.01, 0, 0, 0, 0.01)$, respectively.

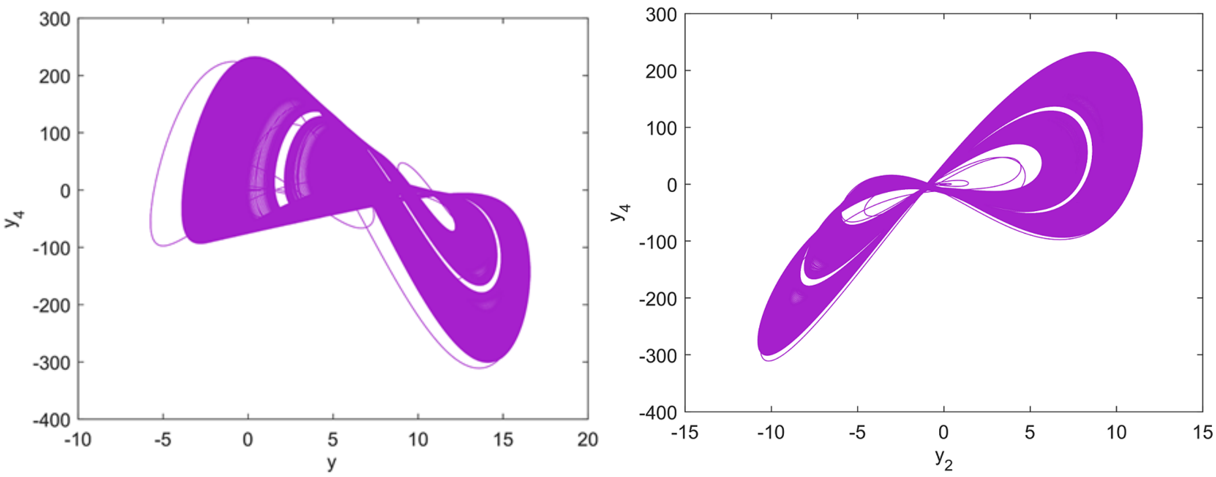

Figure 13. Phase portraits of (3.1) in the $y - y_4$ plane and $y_2 - y_4$ plane, respectively.

From these figures, it can be observed that the synchronization errors converge to zero and the hyperchaotic synchronization of the two systems is achieved rapidly. It should be noted that the coefficients of the function V and controllers c_1–c_5 are chosen such that C is negative definite, and the synchronization rate can be further enhanced through appropriate parameter tuning. The system in [23] achieves synchronization at 30 s, whereas the proposed system accomplishes synchronization at 10 s. Thus, compared with the chaotic system reported in [23], the proposed hyperchaotic system exhibits more complex dynamics, yet the designed nonlinear feedback scheme still enables faster global asymptotic synchronization.

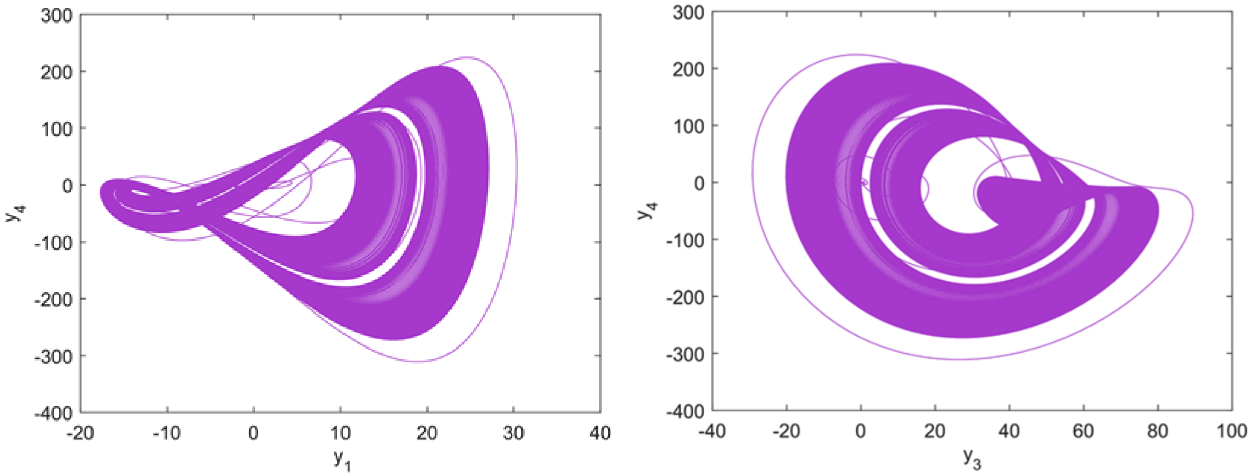

Figure 14. Phase portraits of (3.1) in the $y_1 - y_4$ plane and $y_3 - y_4$ plane, respectively.

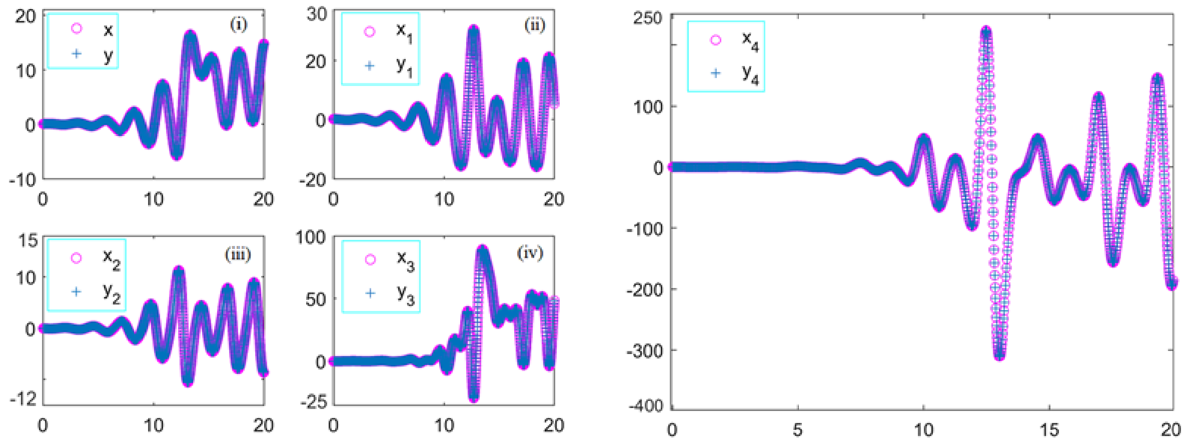

Figure 15. Time evolution of the states $x,\ x_1, x_2,\ x_3,\ x_4$ and $y,\ y_1,\ y_2,\ y_3,\ y_4$, respectively.

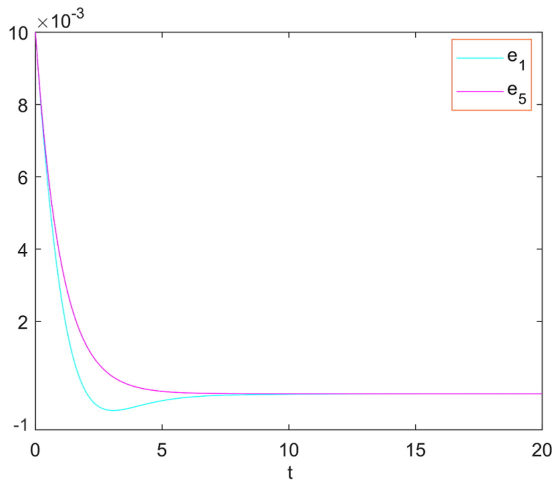

Figure 16. Synchronization errors e_1, e_5 versus time.

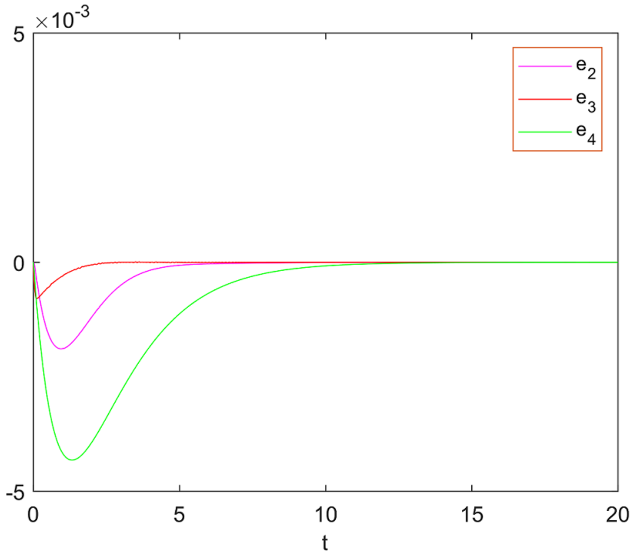

Figure 17. Synchronization errors e_2, e_3, e_4 versus time.

4. Circuit realization

Based on the preceding analysis, it is evident that the new 5D hyperjerk system is capable of generating complex dynamical behaviors. In practical applications, the hardware implementation of theoretical chaotic models plays a pivotal role, particularly in areas such as circuit realization (see [36–38] and the references therein). Accordingly, this section presents a suitable electronic circuit designed to emulate the proposed system (2.1).

By applying the compression transformation

$$x = 10X,\ x_1 = 10X_1,\ x_2 = 10X_2,\ x_3 = 10X_3,\ x_4 = 100X_4,$$

one obtains

$$\begin{cases} \dot{X} = X_1, \\ \dot{X}_1 = aX_2, \\ \dot{X}_2 = -a_1X - a_2X_1 - a_3X_2 + a_4X_3, \\ \dot{X}_3 = -10a_5X_4 - a_6X_3, \\ \dot{X}_4 = X_1X_2 + aX_2^2 + \dfrac{a}{10}X_2 + (X + X_1)\dot{X}_2 - a_0X_4. \end{cases} \tag{4.1}$$

The circuit schematic of (4.1) is given in Figure 18, in which the five channels correspond to the state variables X, X_1, X_2, X_3, and X_4, respectively, and each state variable is labeled in the figure. $U_i\,(i = 1, 2, ..., 15)$ are implemented with the operational amplifier LM675T.

The circuit equations are given as follows:

$$
\begin{cases}
C_1 \frac{dX}{d\tau} = \frac{R_2 X_1}{R_1 R_3}, \\
C_2 \frac{dX_1}{d\tau} = \frac{R_7 X_2}{R_6 R_8}, \\
C_3 \frac{dX_2}{d\tau} = -\frac{R_{12} X}{R_{16} R_{13}} - \frac{R_{12} X_1}{R_{11} R_{13}} - \frac{R_{12} X_2}{R_{13} R_{17}} + \frac{R_{12} X_3}{R_{18} R_{13}}, \\
C_4 \frac{dX_3}{d\tau} = -\frac{R_{20} X_4}{R_{23} R_{19}} - \frac{R_2 X_3}{R_{24} R_{19}}, \\
C_5 \frac{dX_4}{d\tau} = \frac{R_{25} X_2^2}{R_{29} R_{28}} - \frac{R_{25} X^2}{R_{31} R_{28}} - \frac{R_{25} X_1^2}{R_{30} R_{28}} - \frac{R_{25} X X_1}{R_{28} R_{30}} - \frac{R_{25} X X_2}{R_{28} R_{32}} \\
\qquad - \frac{R_{25} X_1 X_2}{R_{33} R_{28}} + \frac{R_{25} X X_3}{R_{34} R_{28}} + \frac{R_{25} X X_3}{R_{36} R_{28}} + \frac{R_{25} X_2}{R_{28} R_{37}} - \frac{R_{25} X_4}{R_{28} R_{38}}.
\end{cases} \tag{4.2}
$$

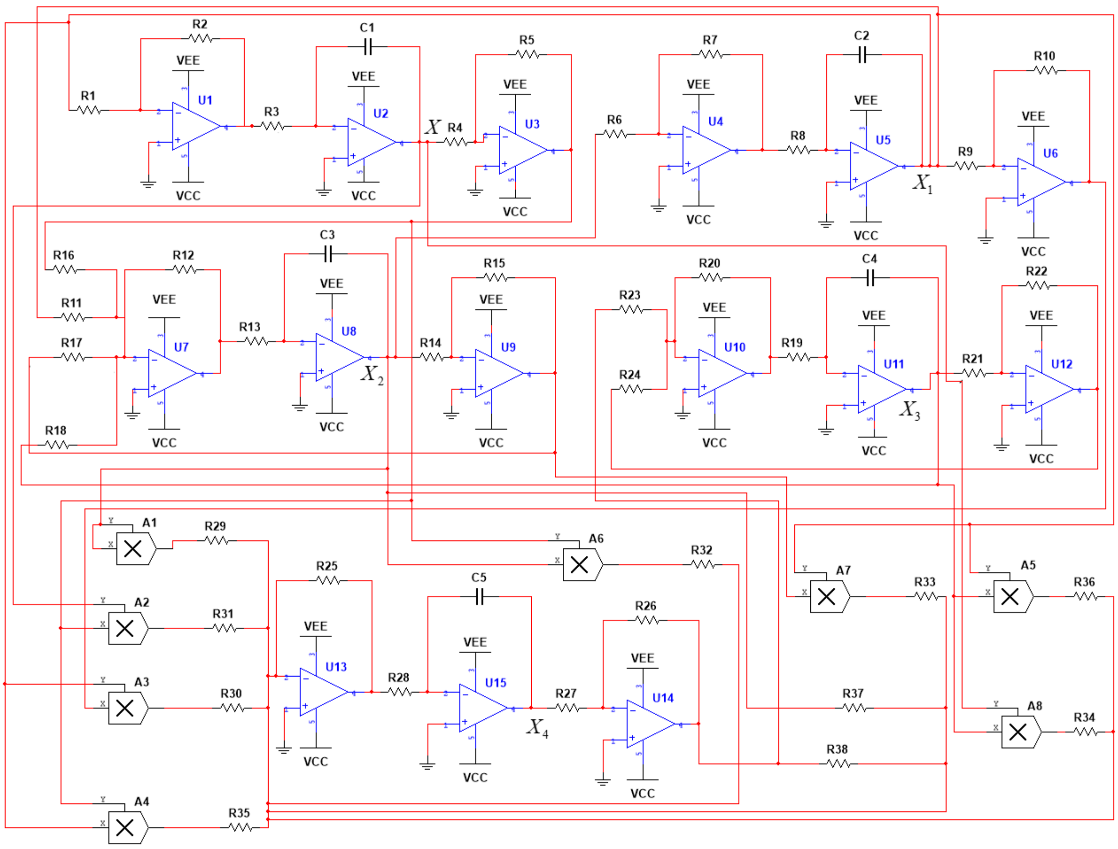

Figure 18. Electronic circuit implementation of the 5D hyperjerk system (2.1).

By equating the coefficients of corresponding variables on the right-hand sides of (4.1) and (4.2) term by term and substituting the hyperchaotic parameter values presented in subsection 2.3, the electronic component values have been selected as follows:

$$R_i = 1K\Omega \, (i = 1, 2, 3, 6, 8, 13, 19, 28),$$

$$R_j = 10K\Omega \, (j = 4, 5, 9, 10, 14, 15, 21, 22, 26, 27),$$

$$C_q = 10\mu F \, (q = 1, 2, 3, 4, 5),$$

$$R_7 = 5.99K\Omega, R_{11} = 610.98K\Omega,$$

$$R_{12} = 336.039K\Omega, R_{16} = 131.78K\Omega,$$

$$R_{17} = 168.86381K\Omega, R_{20} = 9.9K\Omega,$$

$$R_{29} = 17332.92\Omega, R_{38} = 519.12123K\Omega,$$

$$R_{25} = 103.82427K\Omega, R_{18} = 658.9K\Omega,$$

$$R_{23} = 1.1K\Omega, R_{30} = 188771.35\Omega,$$

$$R_{31} = 40715.39\Omega, R_{32} = 52.17298K\Omega,$$

$$R_{33} = 104872.97\Omega, R_{34} = 203576.95\Omega,$$

$$R_{37} = 173329.29\Omega, R_{24} = 18K\Omega,$$

$$R_{35} = 33.40169K\Omega, R_{36} = 203576.95\Omega.$$

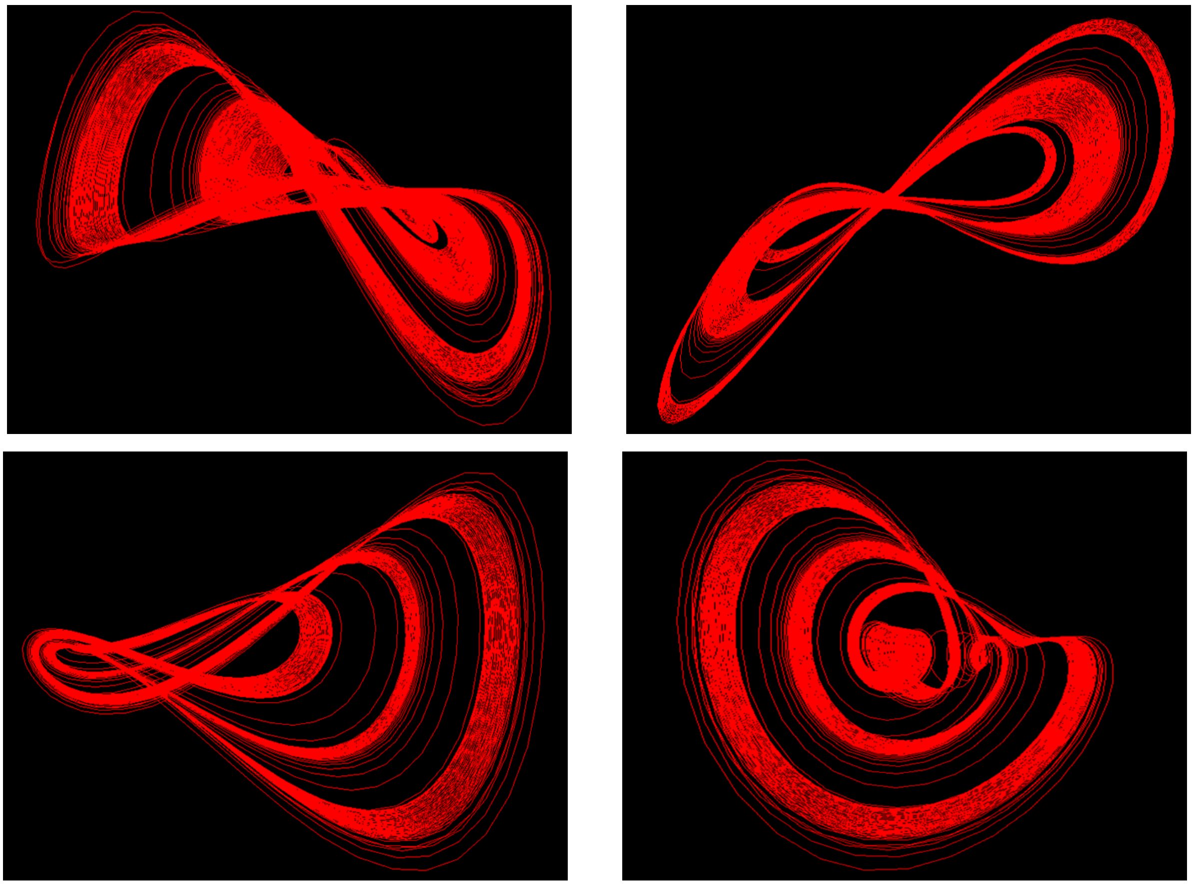

Figure 19. Multisim outputs of the hyperchaotic hyperjerk system (2.1) equivalent circuit.

The power supplies of all active devices are $\pm 25\,V$ and $A_i\,(i = 1, 2, ..., 8)$ are analog multipliers with a gain of one. The experimental time $\tau = RCt\,(R = 1K\Omega,\ C = C_q)$. Figure 19 presents the Multisim circuit simulation results of the proposed hyperchaotic system. Specifically, the phase portraits in the $X - X_4$, $X_2 - X_4$, $X_1 - X_4$, and $X_3 - X_4$ planes are displayed in the upper-left, upper-right, lower-left, and lower-right subfigures, respectively. The circuit simulation outcomes are in good agreement with the numerical simulation results shown in Figures 1 and 2, thereby verifying the correctness of the circuit design and confirming the physical feasibility of the hyperchaotic hyperjerk system. Moreover, since chaotic stream cipher algorithms are extensively applied in industrial scenarios, neglecting the hardware implementability analysis of chaotic systems would impair their engineering practicality [39, 40]. Therefore, prior to designing a stream cipher algorithm based on chaotic systems, it is essential to verify their hardware implementability. After the circuit implementation of (2.1) has been validated, we subsequently investigate its encryption applications.

5. Hyperchaotic encryption and decryption

In this section, we propose image encryption and decryption algorithms based on the hyperchaotic system (2.1). The detailed steps of the image encryption algorithm are as follows:

(i) Set the system parameters as

$$(a, a_1, a_2, a_3, a_4, a_5, a_6, a_0) = (5.99, 2.55, 0.55, 1.99, 0.51, 0.9, 0.55, 0.0002)$$

and the initial state as $(x(0), x_1(0), x_2(0), x_3(0), x_4(0)) = (0.05, 0.1, 0.01, 0.01, 0.02)$.

(ii) Read the plaintext image, where the total number of pixels is $N = H \times W \times D$, with H, W, D representing the height, width, and number of channels of the image, respectively.

(iii) Using the fourth-order Runge-Kutta method, perform $M = 5N + 2000$ iterations on the hyperchaotic system. Then generate a hyperchaotic sequence $h^* = (h_1, h_2, ..., h_N)$, where $h_j = h(s_{1j})$, s_{1j} is the result of rounding $2001 + (M - N - 2001)s_{2j}$ to the nearest integer, and

$s_{2j} = mod(|x_2(t_{M-N+j})|, 1)\,(j = 1, 2, ..., N)$, $h(s_{1j}) = mod(|x_2(t_{s_{1j}})|, 1)\,(j = 1, 2, ..., N)$.

(iv) Sort the sequence $[h^*; h^*]$ in ascending order to obtain a sequence h_* of length $2N$. Select $h_*(m)$, where m represents the rounding of $\frac{(n-1)(2N-1)}{256} + 1$ $(n = 0, 1, 2, ..., 256)$ to the nearest integer. Output the key vector $k^* = (k_1, k_2, ..., k_N)$, where $k_j = min\{n | h_j \le h_*(m)\} - 1,\ j = 1, 2, ..., N$.

(v) Sort the hyperchaotic sequence $S_0 = (s_1, s_2, ..., s_{256})$ in ascending order to obtain the index S_1, and define the S-box: $S(z) = S_1(z) - 1,\ z \in [0, 255]$. Here

$s_j = mod(|x_2(t_j)|, 1)\,(j = 1001, 1002, ..., 1256)$.

(vi) Generate the diffusion key

$$K_1(i) = k_i \oplus \left[\sum_{j=1}^{8} K_0(i, j) 2^{8-j}\right],\ i = 1, 2, ..., N,$$

where k_i is defined in (iv) and $K_0(i, j)$ is defined via $K_2(i, l)$ as follows: $K_0(i, j) = K_2(i, l)$, $K_2(i, l) = \left\lfloor \frac{K(i)}{2^{8-l}} \right\rfloor mod\, 2$, $l = 1, 2, ..., 8$, with $l = 8$ when $j = 1$ and $j = l - 1$ otherwise.

(vii) Reshape the diffusion key into a 3D matrix by setting $K_d(p, q, d) = K_1((d-1)HW + (q-1)W + p)$, and reshape the binary representation into a 4D matrix by setting

$$K_r(p, q, d, r) = K_2((r - 1)HW + (q - 1)W + p, r),$$

where p, q, d, r represent the spatial coordinates, channel index, and bit index of the pixel, respectively.

(viii) Encrypt the original image channel by channel using $E_d(p, q) = S_d^*(p, q) \oplus K_d(p, q, d)$, and output the encrypted image $E = (E_1, E_2, ..., E_D)$. Here, $S_d^*(p, q)$ denotes the matrix obtained by flattening $S_d(p,q) = S(Im_d(p,q)+1) \oplus K_r(p,q,d,1)$ into a vector of length HW, sorting it in ascending order, and then reshaping it. $Im_d(p,q)$ represents all pixels of the d-th channel of the original image.

The decryption process can be briefly summarized as: decrypt channel by channel $S_d^* = E_d(p.q) \oplus K_d(p,q,d) \Rightarrow$ rearrange S_d^* using the inverse index to obtain $S_d \Rightarrow$ obtain the pixels of channel d through inverse S-box substitution $De_d = S^{-1}(S_d(p,q) \oplus K_r(p,q,d,1)+1)$. Finally, output the decrypted image $De = (De_1, De_2, ..., De_d)$.

The effectiveness of the proposed encryption and decryption algorithm is validated by the simulation results presented in Figure 20. As shown, the encrypted image reveals no trace of the original information, confirming that the hyperchaotic secure communication system can effectively safeguard the image during transmission. Moreover, the original image is successfully reconstructed from the encrypted version, underscoring the algorithm's high performance. The statistical analysis is further detailed in Figure 21, where the histograms of the original image (first row) and the encrypted image (second row) are compared. Additionally, the three pairs of subfigures from left to right correspond to the R, G, and B channels, respectively. In each subfigure, the horizontal axis represents the pixel value of the corresponding channel, and the vertical axis represents the statistical frequency of the corresponding pixel values. The uniform distribution observed in the encrypted image's histogram confirms the effectiveness of the encryption process.

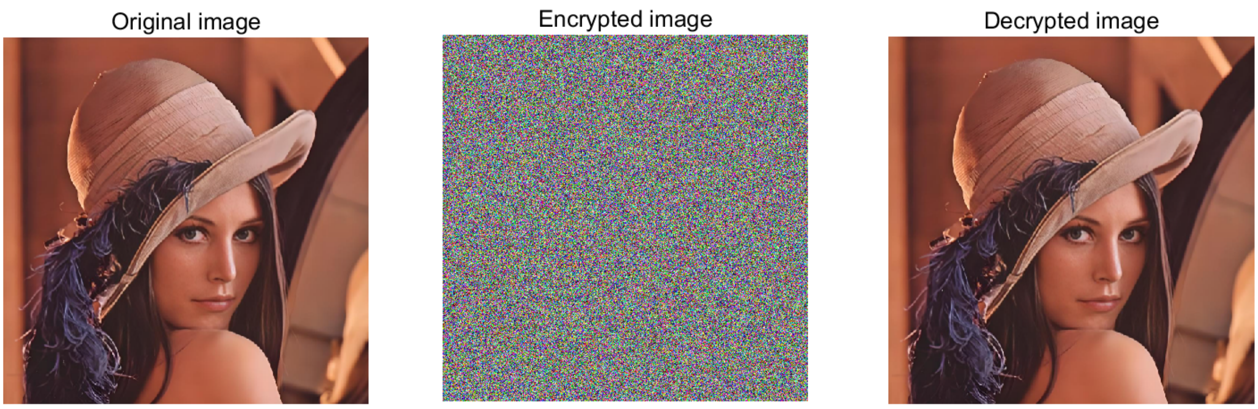

Figure 20. Simulation results of image secure communication.

Figure 22 shows that the key values generated by the algorithm are uniformly distributed, thereby effectively resisting statistical analysis attacks. Here, the horizontal axis represents the values of the keystream, and the vertical axis represents the frequency of occurrence of the corresponding values in the keystream sequence. The distribution of adjacent pixel correlations is presented in Figure 23, where the first row corresponds to the plaintext image and the second row to the encrypted image. It is evident that, for the plain color image, the adjacent pixels in the horizontal, vertical, and diagonal directions across the R, G, and B channels all exhibit strong linear correlations, with the scatter points densely clustered along the diagonal. In contrast, for the cipher-image encrypted by the proposed algorithm, the pixel scatter points in all channels and directions are irregularly and diffusely distributed, and the corresponding correlation coefficients are significantly decreased. This effectively weakens the pixel correlations of the image, thereby resisting statistical analysis and ensuring the security of the image information. Here, the symbols H., V., D. in the figure denote the horizontal, vertical, and diagonal directions, respectively.

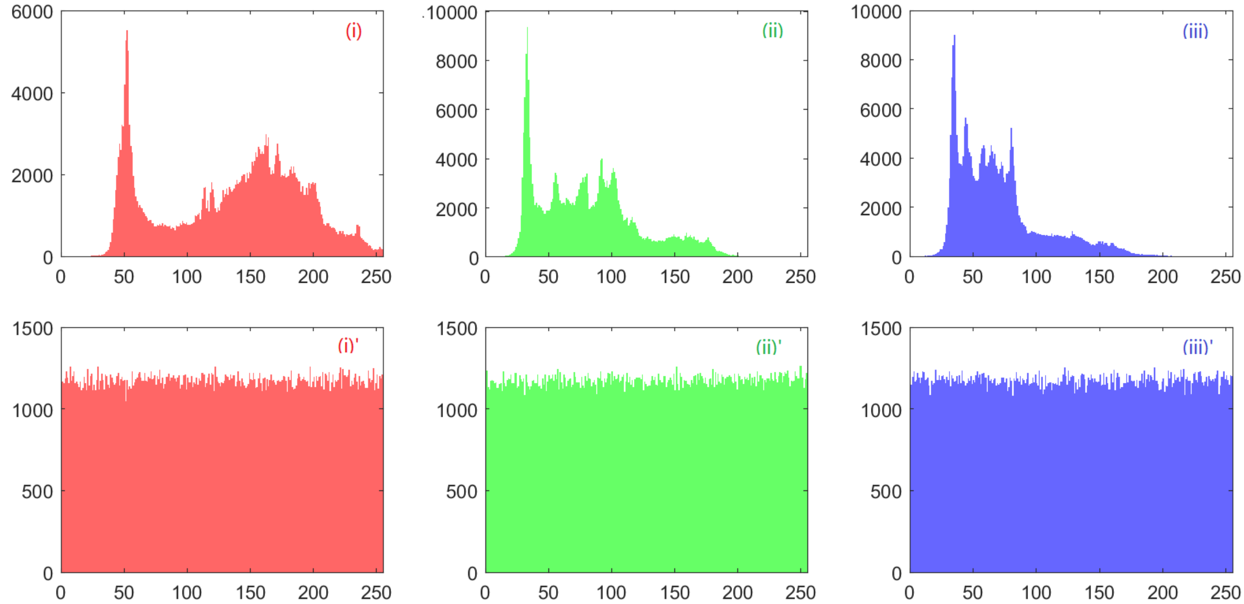

Figure 21. Statistical histograms of the original image and the encrypted image.

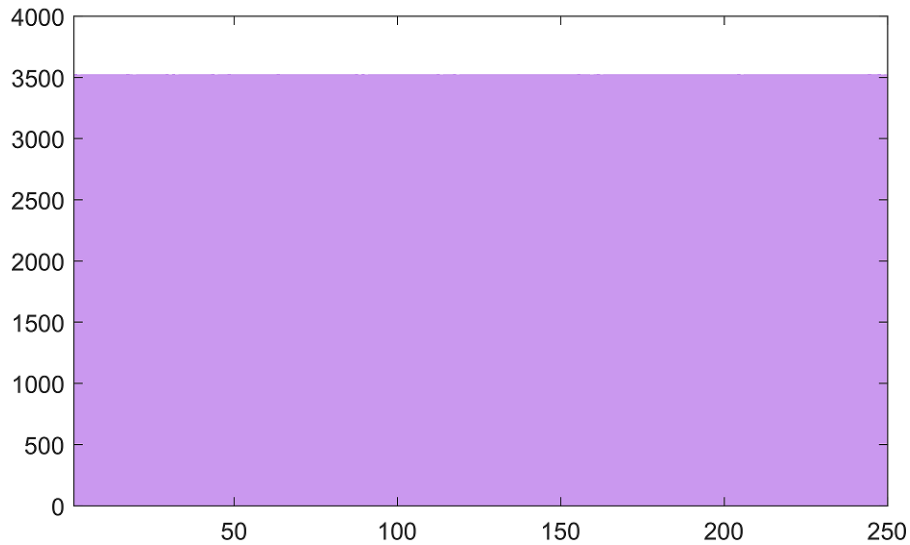

Figure 22. Histogram of the keystream.

Table 1 lists the adjacent pixel correlation coefficients in the horizontal, vertical, and diagonal directions for the R, G, and B channels of the color image encrypted by the proposed algorithm, together with those obtained by several representative existing algorithms. As can be seen from the table, compared with the other encryption schemes, the proposed algorithm yields significantly smaller absolute correlation coefficients in all channels and directions. This indicates that the proposed method effectively weakens the correlations between adjacent pixels, thereby rendering statistical analysis attacks infeasible and providing superior protection for the security of image information. Furthermore, after encryption using the proposed scheme, the information entropy values of the R, G, and B channels of the color image are all 7.9994. These values are extremely close to the theoretical upper bound of 8. An entropy value approaching the theoretical maximum indicates exceptionally high uncertainty in the ciphertext, effectively preventing attackers from reverse-engineering the original image using basic statistical analysis or pattern-recognition techniques. Meanwhile, leveraging the hyperchaotic system defined by (2.1), the proposed encryption scheme achieves a key space of 2^{650}. This key space is far larger than the security threshold required to resist brute-force attacks, and is thus sufficient to withstand exhaustive attacks. Moreover, the number of pixel change rate (NPCR) and unified average changing intensity (UACI) results of the proposed encryption algorithm are 99.6076% and 33.4893%, respectively. Both test results are close to their respective theoretical values, demonstrating that the algorithm can effectively resist differential attacks. In summary, the proposed encryption algorithm exhibits excellent security performance.

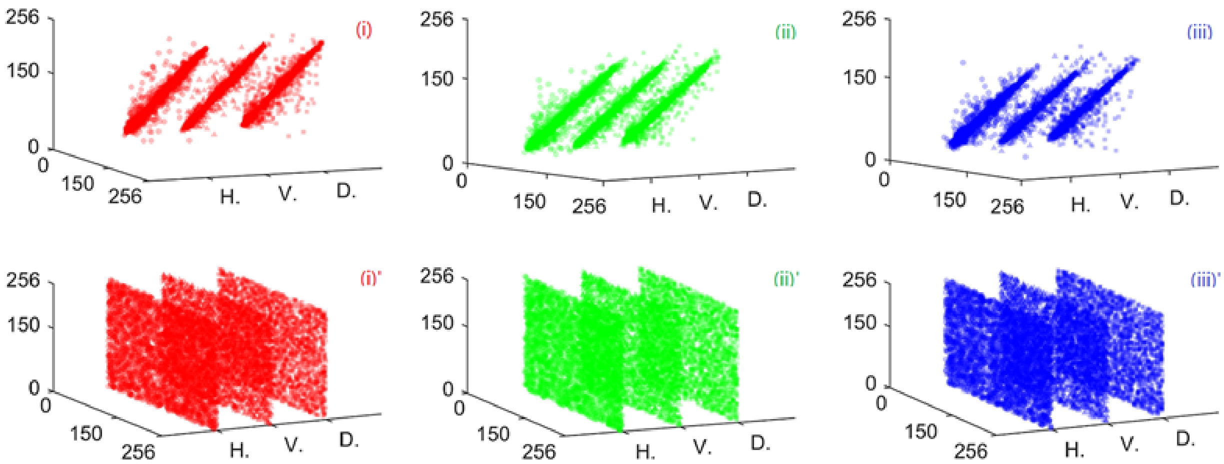

Figure 23. The correlation coefficient graph of the image.

Table 1. Correlation coefficients of the above image encrypted by different algorithms.

Algorithms	Direction	R channel	G channel	B channel
	Horizontal	0.0059	−0.0038	0.0094
[41]	Vertical	−0.0003	−0.0057	0.0133
	Diagonal	−0.0113	−0.0150	−0.0072
	Horizontal	0.0111	−0.0109	−0.0101
[42]	Vertical	−0.0132	0.0175	0.0021
	Diagonal	−0.0016	0.0025	0.0150
	Horizontal	−0.0004	0.0001	0.0018
Proposed algorithm	Vertical	0.0006	−0.0017	−0.0004
	Diagonal	−0.0017	0.0027	−0.0026

6. Conclusions

A new 5D hyperchaotic hyperjerk system is proposed in this paper. The 4D model in [23] can be regarded as a special case of (2.1). The system is dissipative and possesses a unique equilibrium point, and the stability conditions of this equilibrium point are derived. By means of Lyapunov exponents, bifurcation diagrams, the 0-1 test, and Poincaré sections, the hyperchaotic characteristics of the system are investigated, demonstrating that various hyperchaotic attractors can emerge under different parameter conditions. Furthermore, combining normal form theory with symbolic computation, the existence of Hopf bifurcation at the equilibrium point and the stability of the bifurcating solutions are analyzed. The theoretical results are verified through numerical simulations. Based on nonlinear control and Lyapunov stability theory, a nonlinear controller is designed to achieve synchronization of the 5D hyperchaotic hyperjerk system. Simulation results, including phase portraits of the response system, the temporal evolution of state variables, and the error system, indicate that the proposed controller can achieve hyperchaotic synchronization effectively and rapidly. In terms of hardware implementation, an electronic circuit for the five-dimensional hyperchaotic system is designed using 38 resistors and other electronic components. The close agreement between the circuit simulation results and the numerical simulation results confirms the physical realizability of the system. Moreover, from a practical application perspective, the encryption and decryption algorithms based on the hyperchaotic characteristics of the system are designed. Simulation results, in conjunction with key space, NPCR, and UACI analyses, demonstrate that the algorithm possesses good security and strong resistance to attacks. Table 2 compares the research contents of this paper with those of some related works. Among these works, [20, 21, 23] all investigate four-dimensional hyperjerk systems, whereas the five-dimensional hyperjerk system constructed in this work can generate more complex dynamical behaviors, including Hopf bifurcation and hyperchaos. In terms of applications, this study further extends the application scenarios of hyperjerk systems in the field of encryption and decryption. Furthermore, this paper adopts a construction method for hyperjerk systems that differs from those in the references listed in Table 2 and [22, 24, 25], endowing the system with dynamical characteristics distinct from those reported in the related literature. In particular, the Hopf bifurcation behaviors have not been explored in any of the references listed in Table 2, nor in [22, 24]; moreover, the implementation of a hyperchaotic circuit and its application to encryption and decryption have not been investigated in any of the references in Table 2, nor in [22, 24, 25]. In summary, this study not only constructs a new type of hyperchaotic system but also systematically explores its attractors, bifurcations, synchronization, circuit implementation, and encryption applications, thereby enriching the research on hyperjerk systems.

Table 2. Comparison with other references.

	This paper	[20]	[21]	[23]
Dynamic analysis	parameter bifurcation	also studied	also studied	also studied
	Hopf bifurcation	not reported	not reported	not reported
	hyperchaos	chaos	chaos	chaos
Practical application	hyperchaotic circuit	chaotic circuit	not reported	chaotic circuit
	encryption and decryption	not reported	not reported	not reported

Use of AI tools declaration

The authors declare they have not used Artificial Intelligence (AI) tools in the creation of this article.

Acknowledgments

This project was supported by the University Characteristic Innovation Project of Guangdong Province (No. 2023KTSCX079) and by the Doctoral Scientific Research Foundation of Hanshan Normal University (No. QD202130).

Conflict of interest

The authors declare there are no conflicts of interest.

References

1. M. Alawida, A novel image encryption algorithm based on cyclic chaotic map in industrial iot environments, *IEEE Trans. Ind. Inf.*, **20** (2024), 10530–10541. https://doi.org/10.1109/TII.2024.3395631
2. V. Balasubramanian, J. M. Magan, Q. Wu, Quantum chaos, integrability, and late times in the Krylov basis, *Phys. Rev. E*, **111** (2025), 014218. https://doi.org/10.1103/PhysRevE.111.014218
3. M. Tian, S. Yan, Y. Uyaroğlu, A. Mohammadzadeh, H. Taghavifar, C. Zhang, Type-3 fuzzy discrete-time modeling and synchronization of financial chaotic/hyperchaotic systems, *Nonlinear Dyn.*, **113** (2025), 28427–28447. https://doi.org/10.1007/s11071-025-11533-1
4. E. N. Lorenz, Deterministic nonperiodic flow, *J. Atmos. Sci.*, **20** (1963), 130–141. https://doi.org/10.1175/1520-0469(1963)020%3C0130:DNF%3E2.0.CO;2
5. O. E. Rossler, An equation for hyperchaos, *Phys. Lett. A*, **71** (1979), 155–157. https://doi.org/10.1016/0375-9601(79)90150-6
6. J. C. Sprott, Some simple chaotic jerk functions, *Am. J. Phys.*, **65** (1997), 537–543. https://doi.org/10.1119/1.18585
7. G. Chen, T. Ueta, Yet another chaotic attractor, *Int. J. Bifurcation Chaos*, **9** (1999), 1465–1466. https://doi.org/10.1142/S0218127499001024
8. J. Lü, G. Chen, A new chaotic attractor coined, *Int. J. Bifurcation Chaos*, **12** (2002), 659–661. https://doi.org/10.1142/S0218127402004620
9. J. Chen, W. Lv, L. Y. Zhang, Z. Hua, L. Zhang, Z. Zhu, Power-α chaotic system with robust chaos, *Nonlinear Dyn.*, **113** (2025), 12185–12197. https://doi.org/10.1007/s11071-024-10680-1
10. S. Yan, Y. Cui, X. Sun, A jerk chaotic system with bistable locally active memristor and its analysis of multi-scroll formation mechanism, *Eur. Phys. J. Plus*, **139** (2024), 30. https://doi.org/10.1140/epjp/s13360-023-04829-x
11. S. Wang, J. He, Design of new chaotic system with multi-scroll attractor by using variable transformation and its application, *Phys. Scr.*, **100** (2025), 025230. https://doi.org/10.1088/1402-4896/adaa39

12. R. Lan, Y. Wang, T. Xia, L. Lin, Dynamical analysis and FPGA implementation of a memristive non-Hamiltonian conservative hyperchaotic system with extreme multistability, *Integration*, **106** (2026), 102565. https://doi.org/10.1016/j.vlsi.2025.102565

13. Q. Yang, W. M. Osman, C. Chen, A new 6D hyperchaotic system with four positive Lyapunov exponents coined, *Int. J. Bifurcation Chaos*, **25** (2015), 1550060. https://doi.org/10.1142/S0218127415500601

14. K. H. Moussa, A novel hyperchaotic four-dimensional memristive log-logistic sine map with histogram equalisation for image encryption, *Nonlinear Dyn.*, **113** (2025), 31725–31754. https://doi.org/10.1007/s11071-025-11694-z

15. K. Aldwoah, E. I. Hassan, M. Alsharafi, A. F. Alharbi, Hyperchaotic system for secure communication: A modified 4D model and its dynamics, *J. Nonlinear Math. Phys.*, **32** (2025), 90. https://doi.org/10.1007/s44198-025-00348-8

16. C. Zhao, H. Ren, Image encryption based on infinite dimensional hyper-chaotic multi-attractors, *Nonlinear Dyn.*, **100** (2020), 679–698. https://doi.org/10.1007/s11071-020-05526-5

17. K. A. Abed, S. F. Al-Azzawi, O. S. Qasim, Electronic circuit and image encryption using a novel simple 4D hyperchaotic system, *Phys. Scr.*, **100** (2025), 015210. https://doi.org/10.1088/1402-4896/ad941d

18. K. E. Chlouverakis, J. C. Sprott, Chaotic hyperjerk systems, *Chaos, Solitons Fractals*, **28** (2006), 739–746. https://doi.org/10.1016/j.chaos.2005.08.019

19. F. Y. Dalkiran, J. C. Sprott, Simple chaotic hyperjerk systems, *Int. J. Bifurcation Chaos*, **26** (2016), 1650189. https://doi.org/10.1142/S0218127416501893

20. S. Vaidyanathan, F. Hannachi, M. A. Mohamed, A. Sambas, C. Aruna, R. Ramesh, A new chaotic hyperjerk system with a half-line of equilibrium points, its dynamic analysis, multistability, circuit simulation and anti-synchronization via backstepping control, *Arch. Control Sci.*, **35** (2025), 123–143. https://doi.org/10.24425/acs.2025.153960

21. K. Rajagopal, Y. Shekofteh, F. Nazarimehr, C. Li, S. Jafari, A new chaotic multi-stable hyperjerk system with various types of attractors, *Indian J. Phys.*, **96** (2022), 1501–1507. https://doi.org/10.1007/s12648-021-02075-4

22. L. Jiang, J. Li, W. Zhang, Bifurcations and chaos dynamics of a hyperjerk system with antimonotonicity, *Eur. Phys. J. Plus*, **135** (2020), 767. https://doi.org/10.1140/epjp/s13360-020-00786-x

23. E. Zambrano-Serrano, A. Anzo-Hernández, A novel antimonotic hyperjerk system: Analysis, synchronization and circuit design, *Phys. D*, **424** (2021), 132927. https://doi.org/10.1016/j.physd.2021.132927

24. G. D. Leutcho, J. Kengne, L. K. Kengne, A. Akgul, V. Pham, S. Jafari, A novel chaotic hyperjerk circuit with bubbles of bifurcation: Mixed-mode bursting oscillations, multistability, and circuit realization, *Phys. Scr.*, **95** (2020), 075216. https://doi.org/10.1088/1402-4896/ab92da

25. R. Y. Taha, N. H. Hussein, A. I. Amen, Hopf and zero-double Hopf bifurcations of 5D hyperjerk oscillator network system, *Int. J. Bifurcation Chaos*, **35** (2025), 2550029. https://doi.org/10.1142/S0218127425500294

26. B. Bao, M. A. Peol, H. Bao, M. Chen, H. Li, B. Chen, No-argument memristive hyper-jerk system and its coexisting chaotic bubbles boosted by initial conditions, *Chaos, Solitons Fractals*, **144** (2021), 110744. https://doi.org/10.1016/j.chaos.2021.110744

27. B. Zhang, J. Wang, Y. Feng, Z. Zhang, Finite-time projective synchronization of hyperjerk systems modeled with fuzzy recurrent neural networks, *IEEE Trans. Fuzzy Syst.*, **32** (2024), 4482–4495. https://doi.org/10.1109/TFUZZ.2024.3401112

28. S. Vaidyanathan, A. Akgul, S. Kaçar, U. Çavuşoğlu, A new 4-D chaotic hyperjerk system, its synchronization, circuit design and applications in RNG, image encryption and chaos-based steganography, *Eur. Phys. J. Plus*, **133** (2018), 46. https://doi.org/10.1140/epjp/i2018-11872-8

29. X. Wang, S. Vaidyanathan, C. Volos, V. Pham, T. Kapitaniak, Dynamics, circuit realization, control and synchronization of a hyperchaotic hyperjerk system with coexisting attractors, *Nonlinear Dyn.*, **89** (2017), 1673–1687. https://doi.org/10.1007/s11071-017-3542-x

30. Q. Yang, C. Chen, A 5D hyperchaotic system with three positive Lyapunov exponents coined, *Int. J. Bifurcation Chaos*, **23** (2013), 1350109. https://doi.org/10.1142/s0218127413501095

31. S. Iqbal, J. Wang, Analysis of a novel fractional order hyper-chaotic system: Dynamics, stability and synchronization analysis, *Phys. Lett. A*, **555** (2025), 130770. https://doi.org/10.1016/j.physleta.2025.130770

32. A. Wolf, J. B. Swift, H. L. Swinney, J. A. Vastano, Determining Lyapunov exponents from a time series, *Phys. D*, **16** (1985), 285–317. https://doi.org/10.1016/0167-2789(85)90011-9

33. G. A. Gottwald, I. Melbourne, A new test for chaos in deterministic systems, *Proc. R. Soc. A.*, **460** (2004), 603–611. https://doi.org/10.1098/rspa.2003.1183

34. J. Guckenheimer, P. Holmes, *Nonlinear Oscillations, Dynamical Systems, and Bifurcations of Vector Fields*, 1st edition, Springer, 1983. https://doi.org/10.1007/978-1-4612-1140-2

35. Y. A. Kuznetsov, *Elements of Applied Bifurcation Theory*, 2nd edition, Springer, 1998.

36. D. Biswas, T. Banerjee, A simple chaotic and hyperchaotic time-delay system: Design and electronic circuit implementation, *Nonlinear Dyn.*, **83** (2016), 2331–2347. https://doi.org/10.1007/s11071-015-2484-4

37. X. Cai, C. Liu, Y. Wang, H. Zhang, A novel 4D chaotic system with nonhyperbolic hyperbolic shape equilibrium points: analysis, circuit implementation and color image encryption, *Int. J. Mod. Phys. B*, **33** (2019), 1950383. https://doi.org/10.1142/S0217979219503831

38. J. Zhang, E. Liu, Circuit design and image encryption of CNN chaotic system based on memristor, *Eur. Phys. J. B*, **97** (2024), 100. https://doi.org/10.1140/epjb/s10051-024-00743-y

39. Y. Wang, Z. Liu, J. Ma, H. He, A pseudorandom number generator based on piecewise logistic map, *Nonlinear Dyn.*, **83** (2016), 2373–2391. https://doi.org/10.1007/s11071-015-2488-0

40. Y. Wang, Z. Zhang, G. Wang, D. Liu, A pseudorandom number generator based on a 4D piecewise logistic map with coupled parameters, *Int. J. Bifurcation Chaos*, **29** (2019), 1950124. https://doi.org/10.1142/s0218127419501244

41. S. Yan, L. Li, B. Gu, Xi Sun, Y. Ren, Y. Zhang, A color image encryption scheme based on chaotic mapping, chaotic system, and DNA coding, *Appl. Intell.*, **53** (2023), 31181–31206. https://doi.org/10.1007/s10489-023-04759-2

42. K. M. Hosny, S. T. Kamal, M. M. Darwish, A novel color image encryption based on fractional shifted Gegenbauer moments and 2D logistic-sine map, *Visual Comput.*, **39** (2023), 1027–1044. https://doi.org/10.1007/s00371-021-02382-1

Appendix

A. Expressions of θ_{ks} $(k = 0, 1, s = 1, 2)$ in Section 2.4

$$\begin{aligned}
\theta_{01} = {} & (a_0 - 2\,a_3 + a_6)\omega^6 - (aa_0a_2 + aa_2a_6 + a_0{}^2a_3 - a_0{}^2a_6 - a_0a_6{}^2 + a_3a_6{}^2)\omega^4 - (aa_0{}^2a_2a_6 + aa_0a_2a_6{}^2 \\
& + aa_0{}^2a_1 + aa_1a_6{}^2)\omega^2 - 2\,aa_0{}^2a_1a_6{}^2, \\
\theta_{02} = {} & 9\,\omega^{10} + (4\,a_0{}^2 - 6\,aa_2 + 2\,a_0a_3 + 2\,a_0a_6 + 4\,a_3{}^2 + 2\,a_3a_6 + 4\,a_6{}^2)\omega^8 + (a^2a_2{}^2 + 2\,aa_0a_2a_3 \\
& - 4\,aa_0a_2a_6 + 2\,aa_2a_3a_6 + a_0{}^2a_3{}^2 + 2\,a_0{}^2a_3a_6 + a_0{}^2a_6{}^2 + 2\,a_0a_3{}^2a_6 + 2\,a_0a_3a_6{}^2 + a_3{}^2a_6{}^2 - 6\,aa_0a_1 \\
& - 6\,aa_1a_6)\omega^6 + (2\,a^2a_0a_2{}^2a_6 + 2\,aa_0{}^2a_2a_3a_6 + 2\,aa_0{}^2a_2a_6{}^2 + 2\,aa_0a_2a_3a_6{}^2 + 2\,a^2a_0a_1a_2 + 2\,a^2a_1a_2a_6 \\
& + 2\,aa_0{}^2a_1a_3 - 6\,aa_0{}^2a_1a_6 - 4\,aa_0a_1a_3a_6 - 6\,aa_0a_1a_6{}^2 + 2\,aa_1a_3a_6{}^2)\omega^4 + (a^2a_0{}^2a_2{}^2a_6{}^2 \\
& + 2\,a^2a_0{}^2a_1a_2a_6 + 2\,a^2a_0a_1a_2a_6{}^2 + a^2a_0{}^2a_1{}^2 + 2\,a^2a_0a_1{}^2a_6 + a^2a_1{}^2a_6{}^2)\omega^2 + 4\,a^2a_0{}^2a_1{}^2a_6{}^2, \\
\theta_{11} = {} & 3\,\omega^6 + (2\,a_0{}^2 - aa_2 + a_0a_3 + a_3a_6 + 2\,a_6{}^2)\omega^4 + (a_0{}^2a_3a_6 + a_0{}^2a_6{}^2 + a_0a_3a_6{}^2 - aa_0a_1 - aa_1a_6)\omega^2 \\
& + aa_0{}^2a_2a_6{}^2 - aa_0{}^2a_1a_6 - aa_0a_1a_6{}^2, \\
\theta_{12} = {} & 9\,\omega^{10} + (4\,a_0{}^2 - 6\,aa_2 + 2\,a_0a_3 + 2\,a_0a_6 + 4\,a_3{}^2 + 2\,a_3a_6 + 4\,a_6{}^2)\omega^8 + (a^2a_2{}^2 + 2\,aa_0a_2a_3 - 4\,aa_0a_2a_6 \\
& + 2\,aa_2a_3a_6 + a_0{}^2a_3{}^2 + 2\,a_0{}^2a_3a_6 + a_0{}^2a_6{}^2 + 2\,a_0a_3{}^2a_6 + 2\,a_0a_3a_6{}^2 + a_3{}^2a_6{}^2 - 6\,aa_0a_1 - 6\,aa_1a_6)\omega^6 \\
& + (2\,a^2a_0a_2{}^2a_6 + 2\,aa_0{}^2a_2a_3a_6 + 2\,aa_0{}^2a_2a_6{}^2 + 2\,aa_0a_2a_3a_6{}^2 + 2\,a^2a_0a_1a_2 + 2\,a^2a_1a_2a_6 + 2\,aa_0{}^2a_1a_3 \\
& - 6\,aa_0{}^2a_1a_6 - 4\,aa_0a_1a_3a_6 - 6\,aa_0a_1a_6{}^2 + 2\,aa_1a_3a_6{}^2)\omega^4 + (a^2a_0{}^2a_2{}^2a_6{}^2 + 2\,a^2a_0{}^2a_1a_2a_6 \\
& + 2\,a^2a_0a_1a_2a_6{}^2 + a^2a_0{}^2a_1{}^2 + 2\,a^2a_0a_1{}^2a_6 + a^2a_1{}^2a_6{}^2)\omega^2 + 4\,a^2a_0{}^2a_1{}^2a_6{}^2.
\end{aligned}$$

B. Expressions of δ, δ_j $(j = 0, 1, ..., 10)$ in Section 2.4

$$\begin{aligned}
\delta = {} & (aa_0a_2 + aa_1)a_6{}^2 + [aa_2a_0{}^2 + (aa_2a_3 + 3\,aa_1 - a_3)a_0 + aa_1a_3 - aa_2]a_6 + aa_1a_0{}^2 + (aa_1a_3 - aa_2)a_0 - aa_1, \\
\delta_0 = {} & -2\,a^3a_1{}^2(aa_0a_1{}^2a_6\theta_0 + 2), \\
\delta_1 = {} & [a_0a_1{}^3a_6(a_2 - 2\,a_1)\theta_0 - a_0a_1{}^3a_6(4\,a_1 - a_2)\theta_1]a^4 + a_1a_2(a_0a_1{}^2a_6\theta_0 + a_0a_1{}^2a_6\theta_1 + 2)a^3 - 2\,a^2a_1a_2, \\
\delta_2 = {} & [-a_0a_1{}^2a_2a_6(a_1 + a_2)\theta_0 - a_0a_1{}^2a_6(4\,a_1{}^2 - 3\,a_1a_2 + a_2{}^2)\theta_1]a^4 + [-a_0a_1{}^2a_6(a_1a_2 - 6\,a_1a_3 - a_2{}^2)\theta_0 \\
& + a_0a_1{}^2a_2a_6(3\,a_1 - a_2)\theta_1 + 2\,a_1a_2]a^3 + (-2\,a_1a_2 + 8\,a_1a_3)a^2, \\
\delta_3 = {} & [a_0a_1{}^2a_2a_6(a_2 - 2\,a_1)\theta_0 + a_0a_1{}^2a_2a_6(2\,a_1 - 3\,a_2)\theta_1]a^4 + [(a_0a_1{}^2a_6(6\,a_1 - a_2)a_3 - a_0a_1{}^2a_6(2\,a_1a_2 \\
& - 3\,a_2{}^2 + 5\,a_1))\theta_0 + (a_0a_1{}^2a_6(12\,a_1 - a_2)a_3 + a_0a_1{}^2a_6(2\,a_1a_2 + a_2{}^2 - 11\,a_1))\theta_1]a^3 + [a_0a_1{}^2a_6(-3\,a_2a_3 \\
& + 4\,a_1)\theta_0 + a_0a_1{}^2a_6(-a_2a_3 + 4\,a_1)\theta_1 - 4\,a_2a_3 + 6\,a_1]a^2 + (-8\,a_1a_3 + 2\,a_1)a, \\
\delta_4 = {} & 2\,a_0a_1{}^2a_2{}^2a_6(\theta_0 - \theta_1)a^4 + [(a_0a_1a_2a_6(a_1 + 2\,a_2)a_3 + a_0a_1{}^2a_6(2\,a_2{}^2 + 5\,a_1 - 9\,a_2))\theta_0 + (3\,a_0a_1{}^2a_6(4\,a_1 \\
& - a_2)a_3 - a_0a_1{}^2a_6(-2\,a_2{}^2 + 3\,a_1 - 5\,a_2))\theta_1]a^3 + [a_0a_1{}^2a_6(-a_2a_3 - 8\,a_3{}^2 + 4\,a_1 + 4\,a_2)\theta_0 \\
& + (a_0a_1a_2a_6(2\,a_2 - 7\,a_1)a_3 + 4\,a_0a_1{}^2a_6(3\,a_1 - a_2))\theta_1 - 4\,a_2a_3 + 4\,a_1]a^2 + (4\,a_1 + 2\,a_2)a, \\
\delta_5 = {} & [(2\,a_0a_1a_2a_6(a_1 + a_2)a_3 + a_0a_1a_6(14\,a_1{}^2 - a_2{}^2))\theta_0 + (a_0a_1a_6(10\,a_1{}^2 + a_2{}^2) - 2\,a_0a_1a_2a_6(a_1 \\
& - 2\,a_2)a_3)\theta_1]a^3 + [(-8\,a_0a_1{}^2a_6a_3{}^2 + a_0a_1a_6(2\,a_1a_2 - 4\,a_2{}^2 + 23\,a_1)a_3 - a_0a_1a_6(8\,a_1{}^2 - 11\,a_1a_2 \\
& + a_2{}^2))\theta_0 + (a_0a_1a_6(8\,a_1{}^2 + 5\,a_1a_2 - a_2{}^2) - 2\,a_0a_1a_6(8\,a_1 - a_2)a_3{}^2 - a_0a_1a_6(6\,a_1a_2 - 2\,a_2{}^2 \\
& - 17\,a_1)a_3)\theta_1]a^2 + [2\,a_0a_1a_3a_6(a_2a_3 - 6\,a_1)\theta_0 - 4\,a_0a_1{}^2a_3a_6\theta_1 + 2\,a_2 - 8\,a_3]a + 4\,a_3(2\,a_3 - 1), \\
\delta_6 = {} & [2\,a_0a_1a_2a_6(4\,a_1 - a_2)\theta_0 - 2\,a_0a_1a_2a_6(-2\,a_2a_3 + 4\,a_1 + a_2)\theta_1]a^3 + [(-4\,a_0a_1a_6a_3{}^2a_2 - a_0a_1a_6(4\,a_2{}^2 \\
& + 9\,a_1 - 3\,a_2)a_3 + 2\,a_0a_1a_6(3\,a_1a_2 + a_2{}^2 - a_1))\theta_0 + (a_0a_1a_6(15\,a_1 - 17\,a_2)a_3 - 2\,a_0a_1a_6(8\,a_1 \\
& - a_2)a_3{}^2 + 2\,a_0a_1a_2a_6(3\,a_1 - a_2))\theta_1]a^2 + [(2\,a_0a_1a_3{}^2a_6(a_2 + 2\,a_3) - a_0a_1a_6(4\,a_1 + a_2)a_3)\theta_0
\end{aligned}$$

$$
\begin{aligned}
&+(4\,a_0a_1a_6a_3{}^2a_2 - 7\,a_0a_1a_6(4\,a_1 - a_2))\theta_1 - 8\,a_3 - 2]a,\\
\delta_7 &= -a_0a_1a_6[(4\,a^2a_2 + 18\,a - 8)a_3{}^2 - 4\,aa_3{}^3 + (38\,a^2a_1 - 6\,a^2a_2 - 8\,aa_1 + 14\,aa_2)a_3 - 11\,a^2a_1 - 6\,a^2a_2\\
&\quad +4\,aa_1 + 3\,aa_2 - 2]\theta_0 + [8\,aa_0a_1a_3{}^3a_6 + (4\,aa_0a_1a_2a_6 - 8\,aa_0a_1a_6)a_3{}^2 + (4\,aa_0a_1a_2a_6 - 2\,a^2a_0a_1a_2a_6\\
&\quad -24\,aa_0a_1{}^2a_6 - 10\,a_1{}^2a_6a_0a^2)a_3 - 9\,a_1{}^2a_6a_0a^2 + 10\,a^2a_0a_1a_2a_6 - 10\,a_1{}^2a_6a_0a^2 - 3\,aa_0a_1a_2a_6]\theta_1,\\
\delta_8 &= -a_0a_1a_6\{[(14\,a - 16)a_3{}^2 - 8\,aa_3{}^3 + (4 - 16\,a^2a_2 - 13\,a)a_3 - 10\,a^2a_1 + 8\,a^2a_2 + 8\,aa_1 + 6\,aa_2]\theta_1\\
&\quad +[(12\,aa_2 - 7\,a + 4)a_3 - (8\,a + 8)a_3{}^2 + 10\,a^2a_1 + 8\,a^2a_2 + 8\,aa_1 - 6\,aa_2]\theta_0\},\\
\delta_9 &= a_0a_1a_6[(28\,aa_3{}^2 - 20\,aa_3 - 5\,a + 8\,a_3 + 4)\theta_0 + (10\,aa_3 + 16\,a_3{}^2 - 11\,a - 16\,a_3 + 4)\theta_1],\\
\delta_{10} &= -2\,a_0a_1a_6[(10\,aa_3 - 5\,a - 4)\theta_1 + (4 - 5\,a - 8\,a_3)\theta_0].
\end{aligned}
$$

AIMS Press